Electronic Supplementary Information

Highly-Photostable Emissive Thienyl-containing Tris(2,4,6-trichlorophenyl)methyl Radicals

Egor D. Tolkachev,[a] Christina S. Becker,[a] Vasily A. Trukhanov,[b] Nikita O. Dubinets,[b,c] Mikhail B. Zuev,[a,d] Alina A. Sonina,[a] Inna K. Shundrina,[a] Elena G. Bagryanskaya,[a] Dmitry Yu. Paraschuk[b] and Maxim S. Kazantsev[a*]

[a]N.N. Vorozhtsov Novosibirsk Institute of Organic Chemistry SB RAS, 630090, Lavrentieva 9, Novosibirsk, Russia

[b]Faculty of Physics, Lomonosov Moscow State University, 119991, GSP-1, Leninskie Gory, Moscow, Russia

[c]Enikolopov Institute of Synthetic Polymeric Materials, Russian Academy of Science, 117393, Profsoyuznaya 70, Moscow, Russia

[d]Novosibirsk State University, 630090, Pirogova 2, Novosibirsk, Russia

1. Experimental

1.1 Quantum-chemical calculations

Ground-state (D_0) and excited (D1) geometries of the studied radicals were optimized using density functional theory (DFT) with the hybrid B3LYP functional,[1] the 6-31G* basis set[2,3] and unrestricted Kohn-Sham (UKS) wavefunctions.[4] To improve the accuracy of the computed energies, single-point calculations were subsequently performed with the 6-311G* basis set.[5,6] At this level, the energies and spatial distributions of the frontier molecular orbitals, as well as the D_0–D_n electronic transition energies, were evaluated. We additionally tested the PBE0,[7] BHHLYP,[8] and CAM-B3LYP,[9] and M06-2X functionals[10] but the results were less consistent with the experimental data (Table S1 and supplementary note S1). All computations were carried out using the *GAMESS-US* software package.[11]

1.2 Synthesis and Characterization

Dibenzothiophene was synthesized from biphenyl according to literature.[12] Dibenzo[*b*,*d*]thiophen-2-ylboronic acid was obtained from 2-bromodibenzo-thiophene according

to literature.[13] HTTM and TTM were synthesized according to literature.[14] All other reagents and solvents were purchased from commercial sources and used without additional purification. Reaction mixtures were monitored by TLC using Masherey-Nagel Pre-coated TLC-sheets Alugram Xtra SIL G/UV254. For column chromatography Masherey-Nagel Kieselgel 60 was used. Combustion analysis was performed with a CHN-analyzer (EURO EA). NMR spectra were recorded with a Bruker AV 400 and Bruker DRX 500 spectrometers. HRMS were obtained with a Thermo Scientific Double Focusing System high resolution mass-spectrometer. Samples were introduced into mass-spectrometer by direct inlet. Electron ionization with 70 eV energy was used. Measurements of the exact masses of molecular ions were performed with respect to the standard lines of perfluorokerosene. IR spectra were recorded in the transmission mode with a Bruker Tensor 27 FT-IR spectrometer in potassium bromide pellets. Thermogravimetric and differential scanning calorimetry analyses were performed in helium atmosphere using a NETZSCH STA 409 instrument with a heating rate of 10 °C/min. ESR spectra were measured in X-Band (~9.31 GHz for **TTM-DBT** and ~9.87 GHz for other compounds) with a Bruker ELEXSYS E 580 (Bruker Corporation, Billerica, MA, USA) spectrometer in deoxygenated DMSO solutions with concentration 10^{-4} M. Spectrometer was set to 0.3 G modulation amplitude and 100 kHz modulation frequency for TTM-2BT, 1.2 G and 60kHz for **TTM-TP**, 0.5 G and 100 kHz for **TTM-DBT** and 0.4 G and 100 kHz for **TTM-DBT**. Glass capillaries of 100 µL volume were used. Cyclic voltammetry measurements were performed in CH_2Cl_2 solution by computer-controlled P-8nano potentiostat (Elins, Russia) in combination with three-electrode cell (Gamry); 0.1 M tetrabutylammonium hexafluorophosphate was used as supporting electrolyte. Pt, Pt wire and Ag/AgCl were used as working, counter and reference electrodes, respectively. The measurements were standardized by measuring the Red/Ox potential of ferrocene after each compound analysis. Al potentials are reported *vs* Fc/Fc^+ Red/Ox couple. SOMO and SUMO energies were estimated using half-wave potentials according to equations:

$$E_{somo} = -(E_{ox}^{1/2} + 4.8)\ (eV)$$

$$E_{sumo} = -(E_{Red}^{1/2} + 4.8)\ (eV)$$

UV/VIS and PL spectra were recorded in a diluted solution (10^{-5} M) in 1x1 cm quartz cuvettes using a Varian Cary 5000 UV-VIS-NIR and Varian Cary Eclipse spectrophotometers, respectively. The PL QY in solution was measured relatively to rhodamine 6G in ethanol (PLQY = 0.94) as reference standard.[15] The solid solutions were prepared by drop-casting the toluene solutions containing radicals and PMMA/HTTMs with a 5% concentration by weight of the former. The PL QY and PL spectra of solid samples were measured using a 3.3-inch-diameter integrating sphere (Newport 819C-SL-3.3) coupled with a UV-Vis spectrometer (QE Pro, Ocean

Optics). The excitation was performed with a diode laser emitting 405 nm (Laserglow). The detailed experimental procedure is described in ref.[16] The photostability of radicals was studied in acetonitrile solution (10^{-6} M) purged with argon in 1×1 cm quartz cuvettes and irradiated with a white lamp (13 W). PL spectra after irradiation were recorded using Varian Cary Eclipse spectrophotometer and the intensity of emission maxima was monitored (Fig. S46) upon excitation at 365 nm. A graph of the logarithm of normalized fluorescence intensity versus time was plotted, and the characteristic degradation time ($\tau_{1/2}$) was determined as 1/slope of the linear fit. To compare the photodegradation rate among the radicals quantitatively, we took into account the overlap of the radical absorption spectra with the irradiation spectrum (as a function of photon energy) with the use of the correction factor. The latter was set to unity for TTM, 4.37 for TP, 2.43 for BT and 1.44 for DBT (in terms of the number of absorbed photons).

The fluorescence time-resolved measurements were performed using the custom-built setup on the basis of the time-correlated single photon counting technique. The samples of radicals dissolved in acetonitrile or cyclohexane were excited with the use of a pulsed 375-nm diode laser (BDU-SM, Becker &Hickl, Germany) with ~40 ps pulse width and 20 MHz repetition rate. Emission was collected in the ranges of 570-750 nm for **TTM-BT**, **TTM-DBT** and 680-850 nm for **TTM-TP** using a photomultiplier (PMC-100, Becker &Hickl, Germany) and a single-photon counter module (SPC-130EM, Becker & Hickl, Germany).

D_1-D_0 dipole moments difference was evaluated using the Lippert-Mataga equation (1):

$$\Delta\nu = \nu_{abs} - \nu_{fl} = \frac{2(\mu_{D1}-\mu_{D0})^2}{hca^3}\left[\frac{\varepsilon-1}{2\varepsilon+1} - \frac{n^2-1}{2n^2+1}\right] + const \quad (1)$$

Where $\Delta\nu$ is Stokes shift; ν_{abs} and ν_{fl} are wavenumbers corresponding to the maxima of the absorption and fluorescence spectra, respectively; μ_{D1} and μ_{D0} are dipole moments in the excited and ground states, respectively; h is Planck's constant; a is the Onsager radius; ε is the solvent dielectric constant; n is refractive index of the solvent.

Synthesis of target compounds:

2-Bromodibenzo[b,d]thiophene

To a stirred solution of dibenzothiophene (3 g, 16.3 mmol) in dichloromethane (50 ml) a small crystal of iodine (cat. amount) was added followed by the dropwise addition of a bromine solution (0.84 ml, 16.3 mmol of Br_2 in dichloromethane (50 ml)) over 30 min at room temperature. The resulting solution was stirred at room temperature for 2 days. The organic solution was washed with saturated sodium thiosulfate solution (2x50 mL), then dried over anhydrous magnesium

sulfate and concentrated in vacuo. The crude product, obtained as a white powder (3.45 g), was used further without further purification. Yield: 80%.

4-Bromo-2,6-dichlorobenzaldehyde (2)

A mixture of 4-bromobenzaldehyde (**1**) (0.50 g, 2.7 mmol), *N*-chlorosuccinimide (0.90 g, 6.7 mmol), anthranilic acid (0.11 g, 0.8 mmol), palladium(II) acetate (0.06 g, 0.3 mmol), 1,2-dichloroethane (21.6 mL) and trifluoroacetic acid (5.4 mL) was stirred for a day at 60 °C. The reaction mixture was quenched with saturated $NaHCO_3$ (aq) solution (100 mL) and extracted with dichloromethane (3x20 mL). The combined organic extracts were washed with water (150 mL), dried over $MgSO_4$ and the solvent was evaporated in vacuo. The crude residue was purified by column chromatography on silica gel (hexane:EtOAc = 19:1) to obtain **2** as bright yellow powder (0.583 mg). Yield: 85%. IR (KBr): 3103, 3068, 2922, 2895, 2852, 1699, 1568, 1537, 1410, 1362, 1269, 1198, 1180, 1126, 1068, 985, 854, 808, 741, 688, 553, 540, 430 cm^{-1}; ^{1}H-NMR ($CDCl_3$, 500.13 MHz) δ, ppm: 10.40 (s, 1H), 7.56 (s, 2H). ^{13}C-NMR ($CDCl_3$, 125.8 MHz) δ, ppm: 188.0, 137.7, 132.7, 129.1, 127.4: HRMS found: m/z 250.8663, calculated for $C_7H_2OBrCl_2$ m/z 250.8661; Anal. Calcd. (%) for $C_7H_3OBrCl_2$: C, 33.11; H, 1.19; Cl, 27.92. Found: C, 33.40; H, 1.24; Cl, 27.75.

5-Bromo-1,3-dichloro-2-(dichloromethyl)benzene (3)

To a mixture of phosphorus pentachloride (3.40 g, 18.4 mmol) and toluene (20 mL) under an inert atmosphere (Ar) a solution of 4-bromo-2,6-dichlorobenzaldehyde (**2**) (3.60 g, 14.2 mmol) in toluene (20 mL) was added. The mixture was stirred for 24 hours at room temperature, then quenched with saturated $NaHCO_3$ (aq) solution (3x50 mL), extracted with dichloromethane (3x20 mL). The combined organic extracts were dried over $MgSO_4$ and the solvent was evaporated in vacuo. The crude residue was purified by column chromatography on silica gel using hexane as eluent, to obtain **3** as colorless oil (3.78 g). Yield: 85%. IR (KBr): 3113, 3078, 3032, 2925, 1568, 1541, 1435, 1373, 1309, 1223, 1205, 1176, 1132, 1076, 858, 800, 775, 690, 557, 501, 430, 407 cm^{-1}; ^{1}H-NMR ($CDCl_3$, 400.1 MHz) δ, ppm: 7.57 (s, 1H), 7.48 (s, 1H), 7.42 (s, 1H); ^{13}C-NMR ($CDCl_3$, 100.6 MHz) δ, ppm: 134.1, 133.0, 130.9, 124.1, 65.3: HRMS found: m/z 305.8164, calculated for $C_7H_3BrCl_4$ m/z 305.8167; Anal. Calcd. (%) for $C_7H_3BrCl_4$: C, 27.23; H, 0.98; Cl, 45.92. Found: C, 27.37; H, 0.94; Cl, 45.85.

(4-Bromo-2,6-dichlorophenyl)bis(2,4,6-trichlorophenyl)methane (HTTM-Br)

5-Bromo-1,3-dichloro-2-(dichloromethyl)benzene (**3**) (1.43 g, 4.6 mmol), 1,3,5-trichlorobenzene (3.37 g, 18.5 mmol) and $AlCl_3$ (1.36 g, 10.2 mmol) were heated to 80 °C in a sealed vessel until a homogeneous melt was obtained and the mixture was stirred for 1.5 h at 80

°C. After cooling to room temperature a portions of 1M hydrochloric acid (30 mL) and dichloromethane (30 mL) were added. The resulting mixture was extracted with dichloromethane (3x50 mL), the combined organic extracts were dried over $MgSO_4$ and the solvent was evaporated in vacuo. **HTTM-Br** was precipitated as a white powder after the addition of a small portion of hexane. Yield: 40%, (1.10 g). IR (KBr): 3076, 2956, 2924, 1724, 1570, 1543, 1435, 1367, 1248, 1190, 1174, 1142, 1132, 1078, 897, 856, 837, 804, 769, 671, 567, 436 cm^{-1}; ^{1}H-NMR ($CDCl_3$, 400.1 MHz) δ, ppm: 7.48 (d, J=2.08 Hz, 1H), 7.36 (d, J=2.08, 1H), 7.34 (d, J=2.25, 2H), 7.21 (d, J=2.25, 2H), 6.64 (s, 1H); ^{13}C-NMR ($CDCl_3$, 100.6 MHz) δ, ppm: 138.2, 138.0, 137.4, 137.2, 134.5, 133.9 (2 peaks), 132.9, 131.3, 130.1, 128.6, 121.3, 50.0; HRMS found: m/z 593.7236, calculated for $C_{19}H_7BrCl_8$ m/z 593.7234; Anal. Calcd. (%) for $C_{19}H_7BrCl_8$: C, 38.11; H, 1.18; Cl, 47.36. Found: C, 38.27; H, 1.24; Cl, 47.23.

General procedure for the synthesis of HTTM-Ar by the Suzuki cross-coupling reaction

A stirring mixture of **HTTM-Br** (0.30 g, 0.50 mmol), boronic acid (0.55 mmol), toluene (15 mL) and MeOH (5 mL) was purged with Ar for 20 minutes, then $Pd(PPh_3)_4$ (0.03 g, 0.03 mmol), aqueous solution of K_3PO_4 (1.06 g, 5 mmol in 5 mL of H_2O) and 1 drop of Aliquat 336® were successively added. The flask was equipped with reflux condenser and sealed. The reaction mixture was heated at 80 °C in sand bath for 2 days, then cooled to rt. Toluene was evaporated under reduced pressure, the resulting solid was filtered off, washed successively with MeOH, hexane and dried at air. The product was purified by column chromatography on silica gel (hexane : CH_2Cl_2 = 4 : 1) to obtain **HTTM-Ar** as white powder.

(4-[5-Phenylthiophene-2-yl]-2,6-dichloro-phenyl)bis(2,4,6-trichlorophenyl)methane (HTTM-TP)

Yield: 85%. IR (KBr): 3064, 1593, 1576, 1543, 1531, 1468, 1443, 1435, 1419, 1390, 1371, 1331, 1275, 1248, 1192, 1176, 1161, 1142, 1128, 1076, 899, 860, 835, 802, 771, 754, 687, 671, 569, 561, 469, 436 cm^{-1}; ^{1}H-NMR ($CDCl_3$, 400.1 MHz) δ, ppm: 7.61 (m, 1H), 7.59 (m, 1H), 7.57 (d, J=1.97 Hz, 1H), 7.44 (d, J=1.97 Hz, 1H), 7.41-7.34 (m, 4H), 7.32-7.39 (m, J=3.81 Hz, 2H), 7.28 (d, J=3.81 Hz, 1H), 7.23 (d, J=2.21 Hz, 2H), 6.72 (s, 1H); ^{13}C-NMR ($CDCl_3$, 100.6 MHz) δ, ppm: 145.5, 139.7, 138.2, 138.0, 137.9, 137.3, 137.2, 135.3, 134.3, 133.9, 133.7, 133.5, 130.1, 129.2, 128.5, 128.2, 126.8, 125.9, 125.7, 125.1, 124.3, 50.2; HRMS found: m/z 673.8317, calculated for $C_{29}H_{14}Cl_8S$ m/z 673.8319; Anal. Calcd. (%) for $C_{29}H_{14}Cl_8S$: C, 51.37; H, 2.08; Cl, 41.82; S, 4.73. Found: C, 51.67; H, 1.99; Cl, 41.74; S, 4.81.

(4-[Benzo[b]thiophen-2-yl]-2,6-dichloro-phenyl)bis(2,4,6-trichlorophenyl)methane (HTTM-BT)

Yield: 65%. IR (KBr): 3074, 2955, 2922, 2868, 2854, 1593, 1576, 1543, 1525, 1460, 1429, 1371, 1335, 1306, 1246, 1186, 1174, 1157, 1140, 1076, 1018, 899, 856, 833, 818, 804, 791, 769, 744, 723, 708, 669, 563, 499, 438, 422 cm^{-1}; ^{1}H-NMR ($CDCl_3$, 400.1 MHz) δ, ppm: 7.83-7.80 (m, 1H), 7.78-7.75 (m, 1H), 7.66 (d, J=2 Hz, 1H), 7.57 (s, 1H), 7.53 (d, J=2 Hz, 1H), 7.37-7.33 (m, J=2.26 Hz, 4H), 7.23 (d, J=2.26 Hz, 2H), 6.74 (s, 1H); ^{13}C-NMR ($CDCl_3$, 100.6 MHz) δ, ppm: 140.4, 139.8, 138.2, 138.1, 137.9, 137.3, 137.2, 135.4, 134.5, 134.2, 133.8, 130.1, 128.6, 127.7, 126.1, 125.3, 125.0, 124.1, 122.5, 121.4, 50.2; HRMS found: m/z 647.8164, calculated for $C_{27}H_{12}Cl_8S$ m/z 647.8162; Anal. Calcd. (%) for $C_{27}H_{12}Cl_8S$: C, 49.73; H, 1.86; Cl, 43.49; S, 4.92. Found: C, 49.70; H, 1.85; Cl, 43.37; S, 4.78.

(4-[Dibenzo[b,d]thiophen-2-yl]-2,6-dichloro-phenyl)bis(2,4,6-trichlorophenyl)methane (HTTM-DBT)

Yield: 50%. IR (KBr): 3072, 2922, 2852, 1635, 1597, 1576, 1543, 1480, 1429, 1371, 1246, 1194, 1174, 1140, 1074, 1024, 899, 858, 804, 762, 733, 677, 561, 507, 438, 419 cm^{-1}; ^{1}H-NMR ($CDCl_3$, 400.1 MHz) δ, ppm: 8.30 (d, J=1.48 Hz, 1H), 8.23-8.19 (m, 1H), 7.90 (d, J=8.37 Hz, 1H), 7.87-7.84 (m, 1H), 7.68 (d, J=1.97 Hz, 1H), 7.63 (dd, J=8.37 Hz, J=1.74 Hz, 1H), 7.55 (d, J=1.97 Hz, 1H), 7.49-7.47 (m, 2H), 7.38 (t, J=1.93 Hz, 2H), 7.26-7.24 (m, 2H), 6.79 (s, 1H); ^{13}C-NMR ($CDCl_3$, 100.6 MHz) δ, ppm: 142.1, 140.1, 139.9, 138.3, 138.1, 137.9, 137.4, 137.3, 136.4, 135.4, 134.4, 133.8, 133.7, 130.1, 128.8, 128.5, 127.3, 127.1, 125.6, 124.8, 123.5, 123.1, 121.9, 119.9, 50.2; HRMS found: m/z 697.8315, calculated for $C_{31}H_{14}Cl_8S$ m/z 697.8319; Anal. Calcd. (%) for $C_{31}H_{14}Cl_8S$: C, 53.03; H, 2.01; Cl, 40.39; S, 4.57. Found: C, 53.20; H, 2.06; Cl, 40.30; S, 4.43.

Method A for oxidation of HTTM-TP or HTTM-BT into radicals

A solution of **HTTM-TP** or **HTTM-BT** (0.3 mmol) in dry diethyl ether (10 mL) was added to a mixture of sodium hydroxide (0.25 g, 6.3 mmol) in DMSO (5 mL), and the mixture was stirred for 2 days at room temperature, forming a dark blue anion. Then DDQ (0.34 g, 1.5 mmol) was added, and the mixture was stirred for a day in the dark at room temperature. The resulting mixture was extracted with chloroform (3x50 mL) and dried with magnesium sulfate. The solvent was evaporated in vacuo and the residue was purified by column chromatography on silica gel (hexane : CH_2Cl_2 = 4 : 1) to give the radical (**TTM-TP** or **TTM-BT**) as dark green powder.

(4-[5-Phenylthiophene-2-yl]-2,6-dichloro-phenyl)bis(2,4,6-trichlorophenyl)methyl radical (TTM-TP)

The product was obtained from **HTTM-TP**. Yield: 80%. IR (KBr): 3070, 3055, 2955, 2924, 2852, 1572, 1552, 1520, 1462, 1443, 1412, 1392, 1371, 1329, 1300, 1275, 1182, 1136, 1080, 1061, 860, 827, 814, 798, 754, 723, 685, 557, 463, 432 cm^{-1}; HRMS found: m/z 672.8239, calculated for $C_{29}H_{13}Cl_8S^{\bullet}$ m/z 672.8241; Anal. Calcd. (%) for $C_{29}H_{13}Cl_8S^{\bullet}$: C, 51.44; H, 1.94; Cl, 41.89; S, 4.74. Found: C, 51.41; H, 1.84; Cl, 41.82; S, 4.88.

(4-[Benzo[b]thiophen-2-yl]-2,6-dichloro-phenyl)bis(2,4,6-trichlorophenyl)methyl radical (TTM-BT)

The product was obtained from **HTTM-BT**. Yield: 80%. IR (KBr): 3061, 2955, 2922, 2852, 1726, 1570, 1554, 1522, 1458, 1439, 1412, 1383, 1369, 1335, 1306, 1298, 1286, 1238, 1203, 1182, 1155, 1138, 1084, 924, 860, 825, 814, 795, 739, 723, 567, 550, 499, 436, 418 cm^{-1}; HRMS found: m/z 646.8090, calculated for $C_{27}H_{11}Cl_8S^{\bullet}$ m/z 646.8084; Anal. Calcd. (%) for $C_{27}H_{11}Cl_8S^{\bullet}$: C, 49.81; H, 1.70; Cl, 43.56; S, 4.92. Found: C, 49.76; H, 1.80; Cl, 43.48; S, 4.73.

Method B for oxidation of HTTM-DBT into radical

(4-[Dibenzo[b,d]thiophen-2-yl]-2,6-dichloro-phenyl)bis(2,4,6-trichlorophenyl)methyl radical (TTM-DBT)

A mixture of **HTTM-DBT** (0.2 mmol) and potassium *tert*-butoxide (0.18 g, 1.6 mmol) in THF (15 mL) was stirred for a day at room temperature, forming a dark red anion. Then *p*-chloranil (0.3 g, 1.2 mmol) was added, and the mixture was stirred for another day in the dark at room temperature. The solvent was evaporated in vacuo and the residue was purified by column chromatography on silica gel (hexane : CH_2Cl_2 = 7 : 3) to give the radical **TTM-DBT** as dark green powder. Yield: 75%. IR (KBr): 3068, 2953, 2922, 2852, 1574, 1545, 1525, 1475, 1429, 1369, 1284, 1246, 1225, 1180, 1155, 1136, 1082, 1024, 897, 858, 806, 761, 731, 559, 507, 436 cm^{-1}; HRMS found: m/z 696.8240, calculated for $C_{31}H_{13}Cl_8S^{\bullet}$ m/z 696.8241; Anal. Calcd. (%) for $C_{31}H_{13}Cl_8S^{\bullet}$: C, 53.11; H, 1.87; Cl, 40.45; S, 4.57. Found: C, 53.32; H, 1.90; Cl, 40.32; S, 4.44.

1.3 Crystal growth and analysis

Compounds were grown by a solvent vapor diffusion method with ethyl acetate used as solvent and water used as antisolvent. The crystal growth time typically was about 4 days. The crystals were examined using an optical microscope (MC-2, «Micmed»). The X-ray diffraction experiments were performed with a Bruker KAPPA APEX II diffractometer with graphite monochromated MoKα radiation. Integration and scaling of the intensity data were accomplished by SAINT.[17] Absorption corrections were applied using SADABS.[18] The structures were solved

by direct methods with SHELXS-97.[19] Refinement was carried out by the full-matrix least-squares technique with SHELXL[20] in software Olex2.[21] All non-hydrogen atoms were refined anisotropically. Hydrogen atom positions were calculated geometrically and refined isotropically according to the riding model. Crystal structures were analyzed for intermolecular interactions using PLATON[22] and Mercury.[23] Crystallographic data for the structures have been deposited to the Cambridge Crystallographic Data Centre as supplementary publication CCDC no. 2513982 (**TTM-TP**), 2513981 (**TTM-BT**), 2513983 (**TTM-DBT**). Copy of the data can be obtained, free of charge, on application to CCDC, 12 Union Road, Cambridge CB21EZ, UK (fax: +44 122 3336033 or e-mail: deposit@ccdc.cam.ac.uk; internet: www.ccdc.cam.ac.uk). Parameters characterizing data collection and refinement, as well as crystal data, are summarized in Table S5. X-ray data collection for all crystals was carried out at 296(2) K.

2. DFT calculations

Supplementary note S1. DFT calculations with different functionals

First, the energies of the half-occupied orbitals were evaluated using several DFT functionals. Comparison with our experimental data indicated that the B3LYP functional provides the best overall agreement. In addition, $D_1 \rightarrow D_0$ transition energies were calculated using different classes of functionals, including hybrid (B3LYP), long-range corrected (CAM-B3LYP), and meta-hybrid (M06-2X) approaches. Consistently, B3LYP yielded the closest agreement with the experiment for these transitions as well.

Table S1. DFT calculations with different functionals.

	TTM-TP	**TTM-BT**	**TTM-DBT**	**TTM-TP**	**TTM-BT**	**TTM-DBT**
	B3LYP/6-311G*			**PBE0/6-311G***		
SOMO, eV	–5.44	–5.56	–5.58	–5.83	–5.97	–5.98
SUMO, eV	–3.39	–3.44	–3.38	–3.36	–3.41	–3.34
Spin contamination (D_0/D_1)	0.023/ 0.035	0.022/ 0.033	0.021/ 0.026	0.033/ -	0.032/ -	0.029/ -
D_1-D_0, nm	814.9	729.7	636.6	-	-	-
	BH&HLYP/6-311G*			**CAM-B3LYP/6-311G***		
SOMO, eV	–6.39	–6.58	–6.62	–6.67	–6.83	–6.85
SUMO, eV	–2.10	–2.14	–2.07	–2.13	–2.17	–2.10
Spin contamination (D_0/D_1)	0.110/ -	0.102/ -	0.091/ -	0.046/ 0.072	0.044/ 0.075	0.041/ 0.065
D_1-D_0, nm	-	-	-	844.7	703.8	566.7
	M06-2X/6-311G*			**Experimental data**		
SOMO, eV	–6.68	–6.80	–6.81	–5.28	–5.41	–5.43
SUMO, eV	–2.69	–2.73	–2.65	–3.80	–3.80	–3.80
Spin contamination (D_0/D_1)	0.019/ 0.024	0.019/ 0.027	0.018/ 0.026			
D_1-D_0, nm	683.5	617.8	558.4	805	745	680

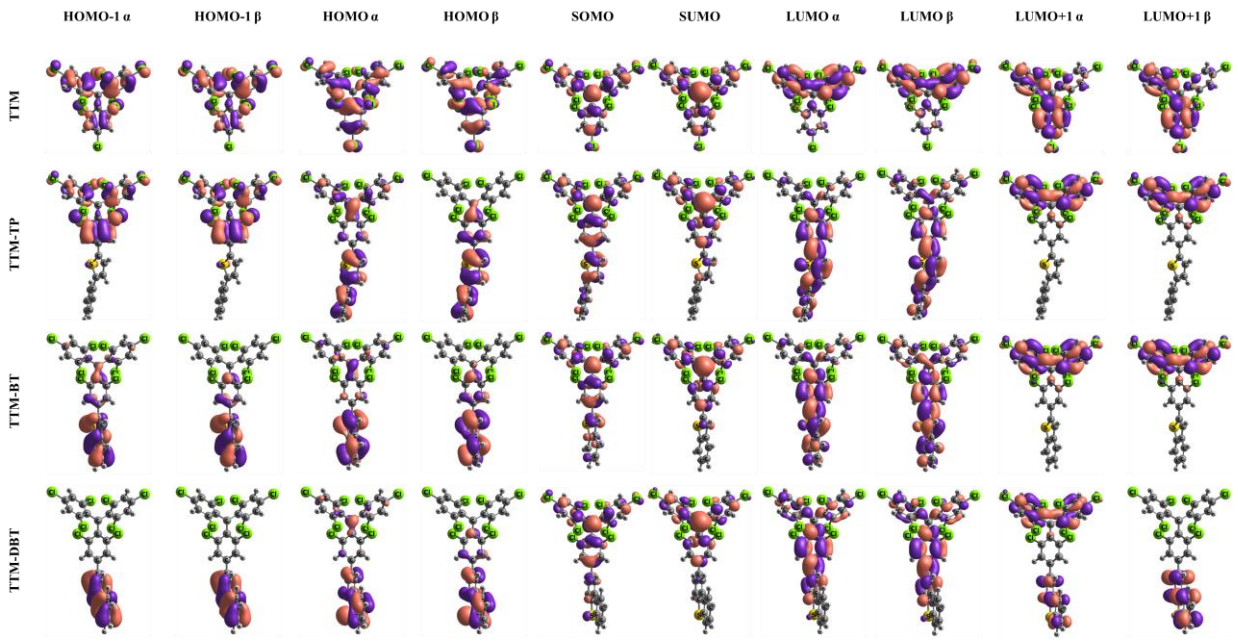

Figure S1. Patterns of molecular orbitals of the radicals studied.

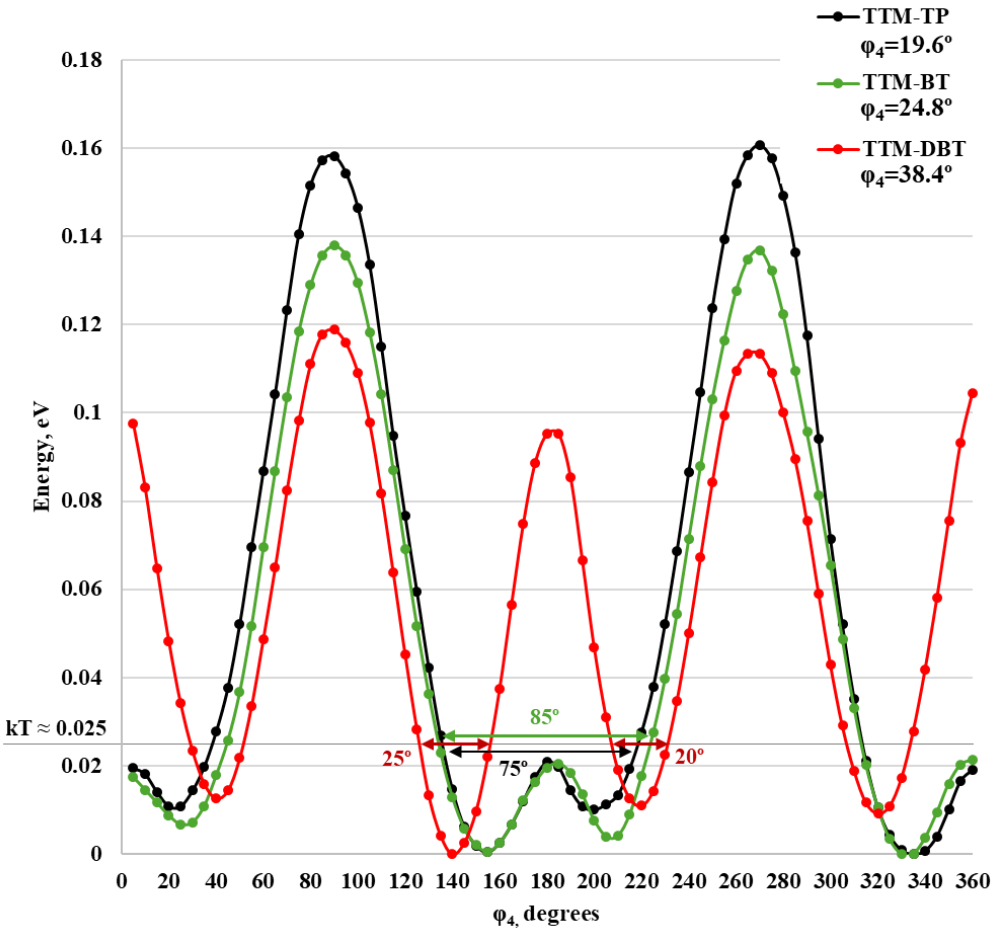

Figure S2. The total energy as a function of the torsion angle φ_4. The lower maxima for **TTM-TP** and **TTM-BT** than those for **TTM-DBT** are assigned to the lower repulsion energy corresponding to one (**TTM-TP**, **TTM-BT**) and two (**TTM-DBT**) pairs of hydrogen atoms belonging to the TTM and the donor moiety. Horizontal arrows show torsional freedom for thermal energy at room temperature for TTM-TP: 75°, TTM-BT: 85°, TTM-DBT: 25° and 20°.

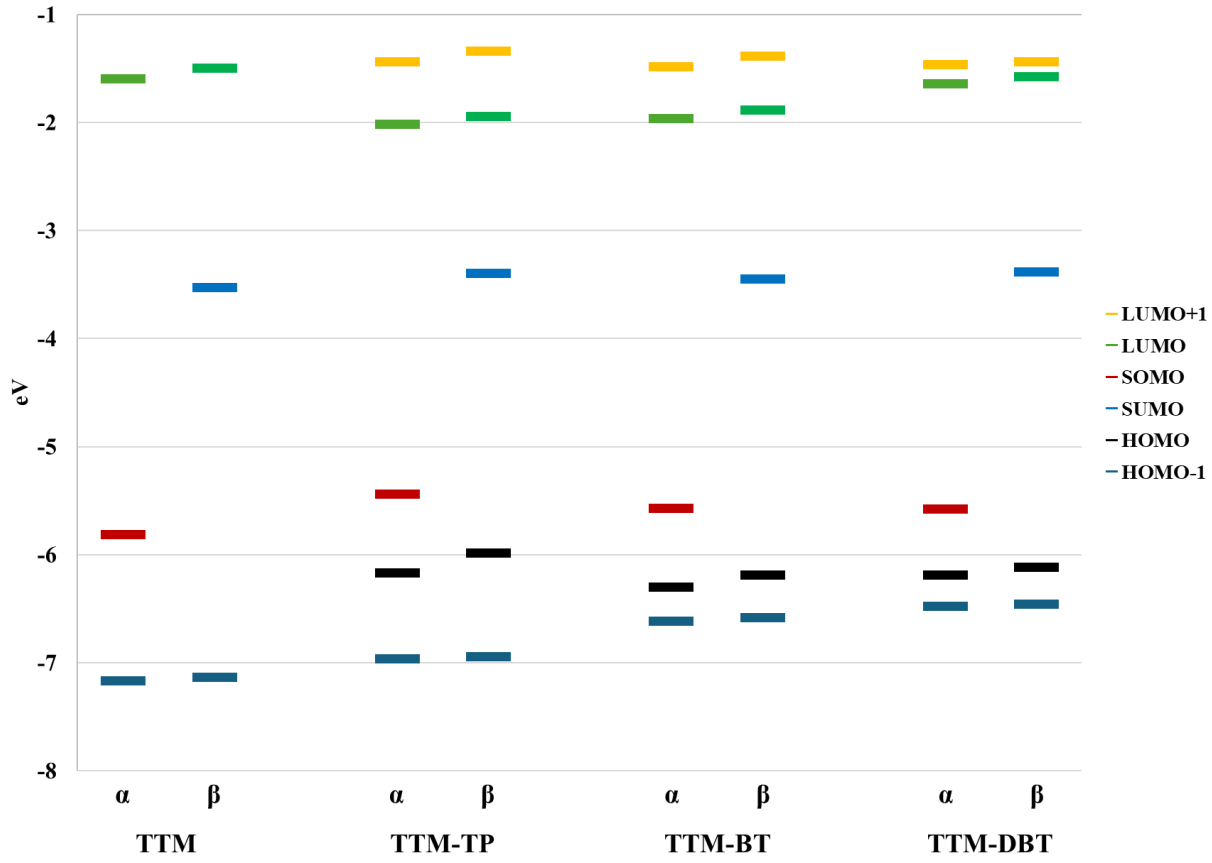

Figure S3. The HOMO–1/HOMO/SUMO/SOMO/LUMO/LUMO+1 energies of the radicals studied.

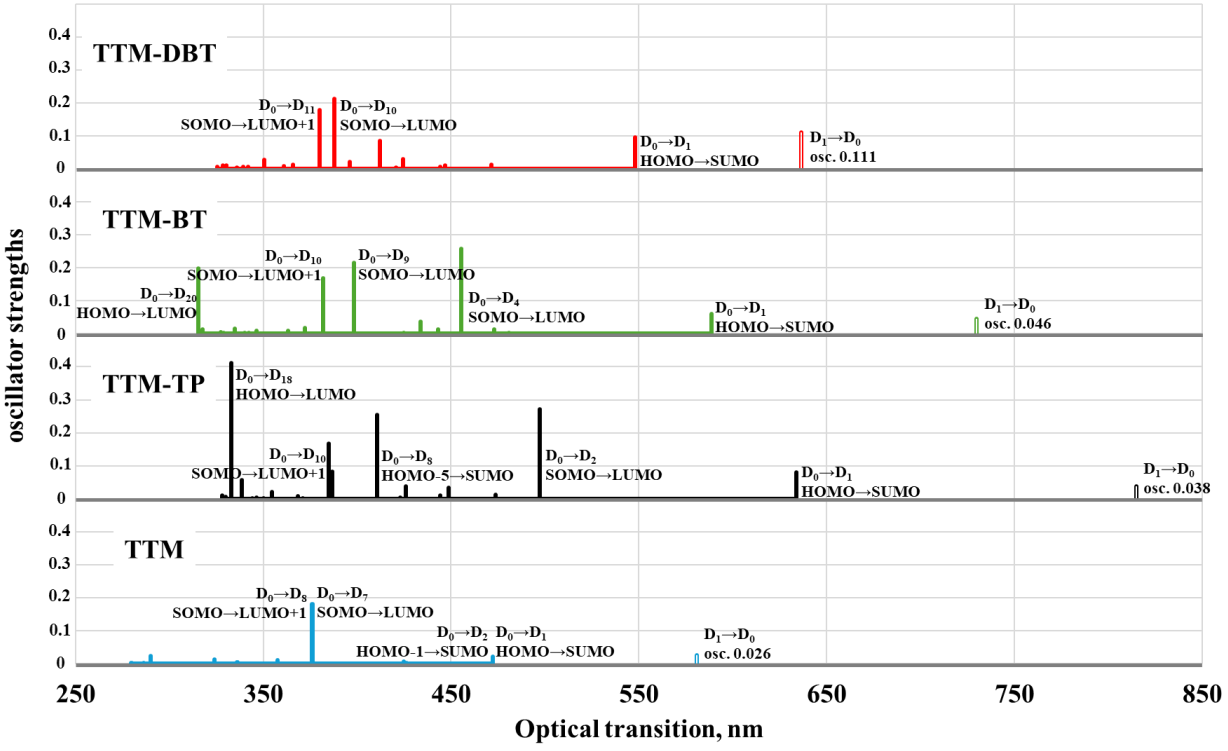

Figure S4. Optical transitions with the corresponding oscillator strengths for the radicals studied.

Table S2. Calculated (B3LYP/6-311G*) values of the lowest energy transitions of studied radicals.

	Calculated transition energy (nm) and oscillator strength	Orbital excitation contribution (≥ 0.2)
TTM	472.41 (D0→D1) osc. 0.021	136β (HOMO) → 137β (SUMO) 0.830818 135β (HOMO–1) → 137β (SUMO) 0.312584 137α (SOMO) → 139α (LUMO+1) 0.291195
	472.32 (D0→D2) osc. 0.021	135β (HOMO–1) → 137β (SUMO) 0.830476 136β (HOMO) → 137β (SUMO) 0.313175 137α (SOMO) → 138α (LUMO) 0.291566
	426.36 (D0→D3) osc. 0.002	133β (HOMO–3) → 137β (SUMO) 0.897292 136β (HOMO) → 137β (SUMO) 0.292807 137α (SOMO) → 139α (LUMO+1) 0.208908
	426.21 (D0→D4) osc. 0.002	132β (HOMO–4) → 137β (SUMO) 0.898069 135β (HOMO–1) → 137β (SUMO) 0.294220 137α (SOMO) → 138α (LUMO) 0.210626
	424.90 (D0→D5) osc. 0.006	134β (HOMO–2) → 137β (SUMO) 0.968854
	376.28 (D0→D7) osc. 0.179	137α (SOMO) → 138α (LUMO) 0.801921 132β (HOMO–4) → 137β (SUMO) 0.315651 135β (HOMO–1) → 137β (SUMO) 0.294861
	376.05 (D0→D8) osc. 0.180	137α (SOMO) → 139α (LUMO+1) 0.801877 133β (HOMO–3) → 137β (SUMO) 0.313834 136β (HOMO) → 137β (SUMO) 0.295193
TTM-TP	633.87 (D0→D1) osc. 0.081	169β (HOMO) → 170β (SUMO) 0.861144 170α (SOMO) → 171α (LUMO) 0.361467 169β (HOMO) → 171β (LUMO) 0.223908
	497.33 (D0→D2) osc. 0.272	170α (SOMO) → 171α (LUMO) 0.603114 169β (HOMO) → 171β (LUMO) 0.468826 169β (HOMO) → 170β (SUMO) 0.451683 169α (HOMO) → 171α (LUMO) 0.329250

	473.59 (D0→D3) osc. 0.013	168β (HOMO–1) → 170β (SUMO) 0.813374 166β (HOMO–3) → 170β (SUMO) 0.362543 170α (SOMO) → 172α (LUMO+1) 0.281366
	448.57 (D0→D4) osc. 0.034	167β (HOMO–2) → 170β (SUMO) 0.770613 170α (SOMO) → 171α (SUMO) 0.266751
	444.23 (D0→D5) osc. 0.009	166β (HOMO–3) → 170β (SUMO) 0.776407 168β (HOMO–1) → 170β (SUMO) 0.468612
	425.77 (D0→D6) osc. 0.038	164β (HOMO–5) → 170β (SUMO) 0.621474 167β (HOMO–2) → 170β (SUMO) 0.478318 170α (SOMO) → 171α (LUMO) 0.296835 169α (HOMO) → 171α (LUMO) 0.245114 169β (HOMO) → 171β (LUMO) 0.224498 170α (SOMO) → 174α (LUMO+3) 0.221483
	410.55 (D0→D8) osc. 0.254	164β (HOMO–5) → 170β (SUMO) 0.463277 161β (HOMO–8) → 170β (SUMO) 0.454905 170α (SOMO) → 171α (LUMO) 0.417475 169β (HOMO) → 171β (LUMO) 0.330878 169α (HOMO) → 171α (LUMO) 0.254026 163β (HOMO–6) → 170β (SUMO) 0.236472
	386.73 (D0→D9) osc. 0.082	161β (HOMO–8) → 170β (SUMO) 0.585209 164β (HOMO–5) → 170β (SUMO) 0.372932 170α (SOMO) → 171α (LUMO) 0.273225 160β (HOMO–9) → 170β (SUMO) 0.247807 169β (HOMO) → 171β (LUMO) 0.215845
	385.05 (D0→D10) osc. 0.167	170α (SOMO) → 172α (LUMO+1) 0.790140 166β (HOMO–3) → 170β (SUMO) 0.317780 165β (HOMO–4) → 170β (SUMO) 0.274865 169α (HOMO) → 172α (LUMO+1) 0.214643
TTM-BT	588.72 (D0→D1) osc. 0.060	162β (HOMO) → 163β (SUMO) 0.859695 163α (SOMO) → 164α (LUMO) 0.321416 162β (HOMO) → 164β (LUMO) 0.196459 161β (HOMO–1) → 163β (SUMO) 0.191056
	480.94 (D0→D2) osc. 0.004	161β (HOMO–1) → 163β (SUMO) 0.762558 160β (HOMO–2) → 163β (SUMO) 0.407888 162β (HOMO) → 163β (SUMO) 0.279082 163α (SOMO) → 164α (LUMO) 0.201662

	473.05 (D0→D3) osc. 0.013	160β (HOMO–2) → 163β (SUMO) 0.738087 161β (HOMO–1) → 163β (SUMO) 0.355395 163α (SOMO) → 165α (LUMO+1) 0.262791 159β (HOMO–3) → 163β (SUMO) 0.245124 158β (HOMO–4) → 163β (SUMO) 0.239207
	455.49 (D0→D4) osc. 0.258	163α (SOMO) → 164α (LUMO) 0.622878 162β (HOMO) → 164β (LUMO) 0.412650 162β (HOMO) → 163β (SUMO) 0.358218 162α (HOMO) → 164α (LUMO) 0.300159 158β (HOMO–4) → 163β (SUMO) 0.207308
	442.96 (D0→D5) osc. 0.013	159β (HOMO–3) → 163β (SUMO) 0.787557 160β (HOMO–2) → 163β (SUMO) 0.425818 158β (HOMO–4) → 163β (SUMO) 0.228495
	433.82 (D0→D6) osc. 0.038	158β (HOMO–4) → 163β (SUMO) 0.799170 161β (HOMO–1) → 163β (SUMO) 0.352435 159β (HOMO–3) → 163β (SUMO) 0.224219
	398.28 (D0→D9) osc. 0.215	163α (SOMO) → 164α (LUMO) 0.506947 162α (HOMO) → 164α (LUMO) 0.435445 162β (HOMO) → 164β (LUMO) 0.416789 156β (HOMO–6) → 163β (SUMO) 0.338569 155β (HOMO–7) → 163β (SUMO) 0.290804
	381.96 (D0→D10) osc. 0.169	163α (SOMO) → 165α (LUMO+1) 0.800391 157β (HOMO–5) → 163β (SUMO) 0.265349 159β (HOMO–3) → 163β (SUMO) 0.261227 160β (HOMO–2) → 163β (SUMO) 0.222878
TTM-DBT	547.88 (D0→D1) osc. 0.095	175β (HOMO) → 176β (SUMO) 0.908448 172β (HOMO–3) → 176β (SUMO) 0.291909 176α (SOMO) → 177α (LUMO) 0.179219
	471.43 (D0→D2) osc. 0.013	173β (HOMO–2) → 176β (SUMO) 0.758769 171β (HOMO-4) → 176β (SUMO) 0.442136 176α (SOMO) → 178α (LUMO+1) 0.224074
	465.24 (D0→D3) osc. 0.001	174β (HOMO–1) → 176β (SUMO) 0.801028 172β (HOMO–3) → 176β (SUMO) 0.360613 175β (HOMO) → 176β (SUMO) 0.299493 176α (SOMO) → 177α (LUMO) 0.192141
	446.79 (D0→D4) osc. 0.010	172β (HOMO–3) → 176β (SUMO) 0.642690 174β (HOMO–1) → 176β (SUMO) 0.509923 176α (SOMO) → 177α (LUMO) 0.269611 168β (HOMO–7) → 176β (SUMO) 0.243516

		175β (HOMO) → 176β (SUMO) 0.213413
	444.23 (D0→D5) osc. 0.006	171β (HOMO–4) → 176β (SUMO) 0.718383 173β (HOMO–2) → 176β (SUMO) 0.551484
	424.46 (D0→D6) osc. 0.030	170β (HOMO–5) → 176β (SUMO) 0.773417 176α (SOMO) → 177α (LUMO) 0.428618 172β (HOMO–3) → 176β (SUMO) 0.254691
	412.18 (D0→D8) osc. 0.086	168β (HOMO–7) → 176β (SUMO) 0.568832 170β (HOMO–5) → 176β (SUMO) 0.346650 176α (SOMO) → 177α (LUMO) 0.309584 174β (HOMO–1) → 178β (LUMO+1) 0.269477
	395.99 (D0→D9) osc. 0.022	168β (HOMO–7) → 176β (SUMO) 0.468788 167β (HOMO–8) → 176β (SUMO) 0.401284 170β (HOMO–5) → 176β (SUMO) 0.315288 174β (HOMO–1) → 178β (LUMO+1) 0.310866 172β (HOMO–3) → 176β (SUMO) 0.293417
	387.70 (D0→D10) osc. 0.213	176α (SOMO) → 177α (LUMO) 0.599217 174β (HOMO–1) → 178β (LUMO+1) 0.349396 174α (HOMO–1) → 179α (LUMO+2) 0.299106 172β (HOMO–3) → 176β (SUMO) 0.298604 170β (HOMO–5) → 176β (SUMO) 0.285666 174α (HOMO–1) → 178α (LUMO+1) 0.251923
	379.97 (D0→D11) osc. 0.178	176α (SOMO) → 178α (LUMO+1) 0.627807 176α (SOMO) → 179α (LUMO+2) 0.487437 171β (HOMO–4) → 176β (SUMO) 0.352000 169β (HOMO–6) → 176β (SUMO) 0.258538

3. Characterization

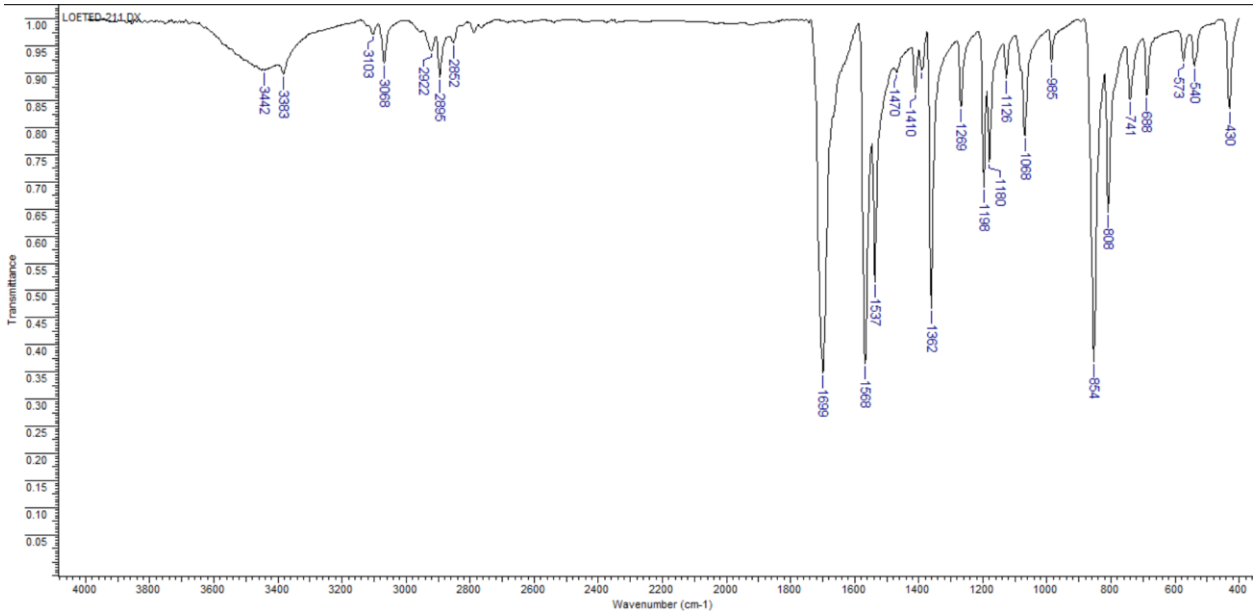

Figure S5. IR spectrum of 4-bromo-2,6-dichlorobenzaldehyde (**2**) in KBr pellets.

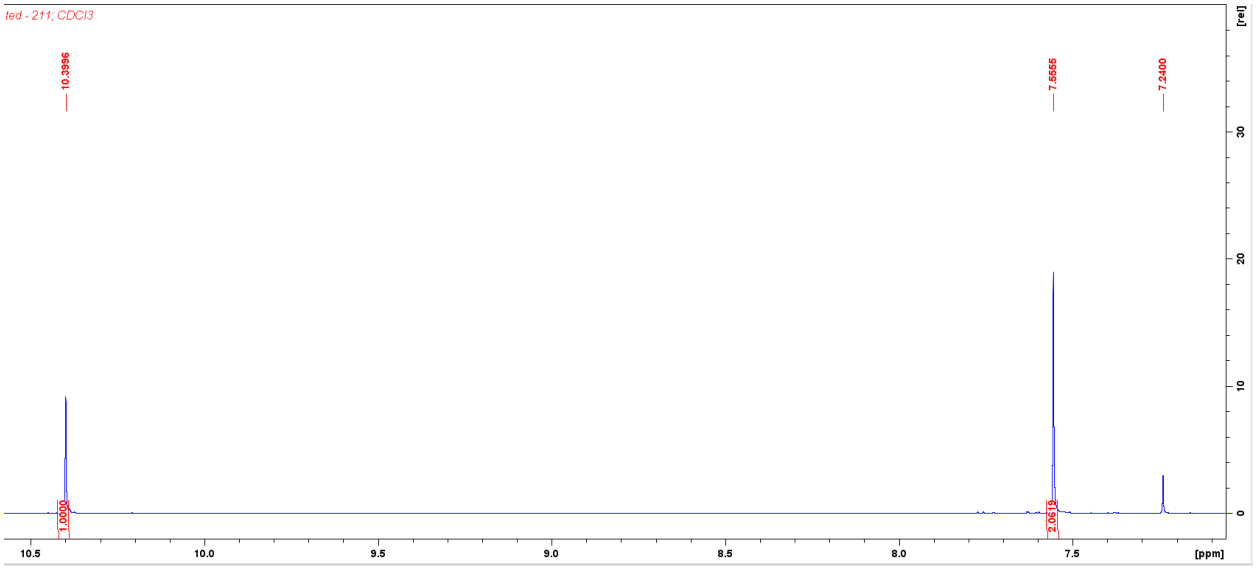

Figure S6. ^{1}H NMR spectrum of 4-bromo-2,6-dichlorobenzaldehyde (**2**) in $CDCl_3$.

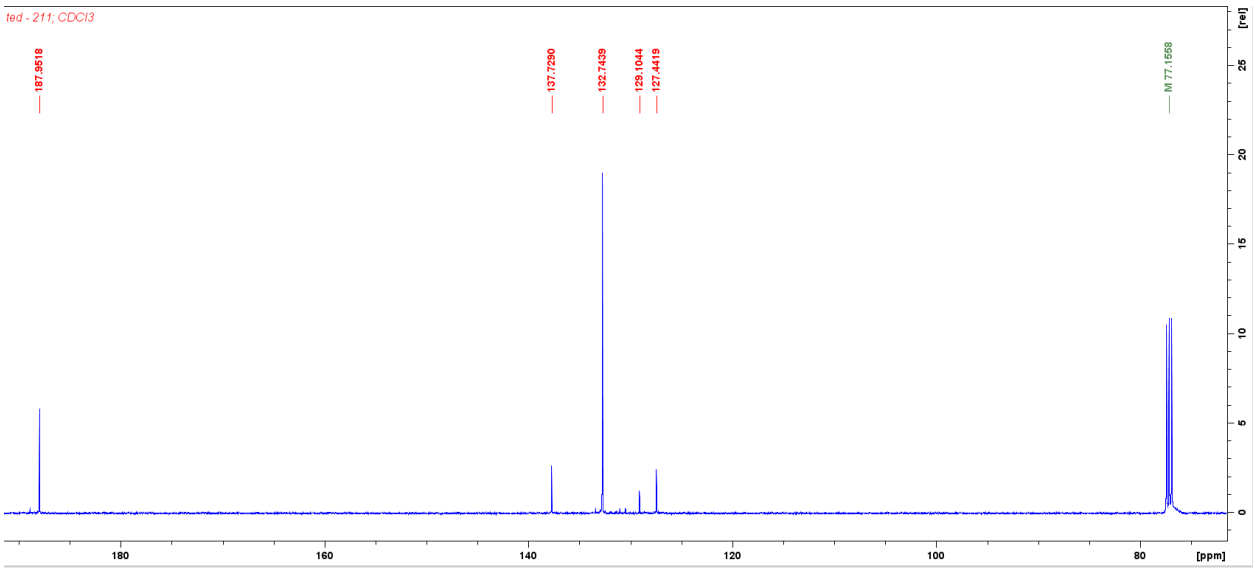

Figure S7. ^{13}C NMR spectrum of 4-bromo-2,6-dichlorobenzaldehyde (**2**) in $CDCl_3$.

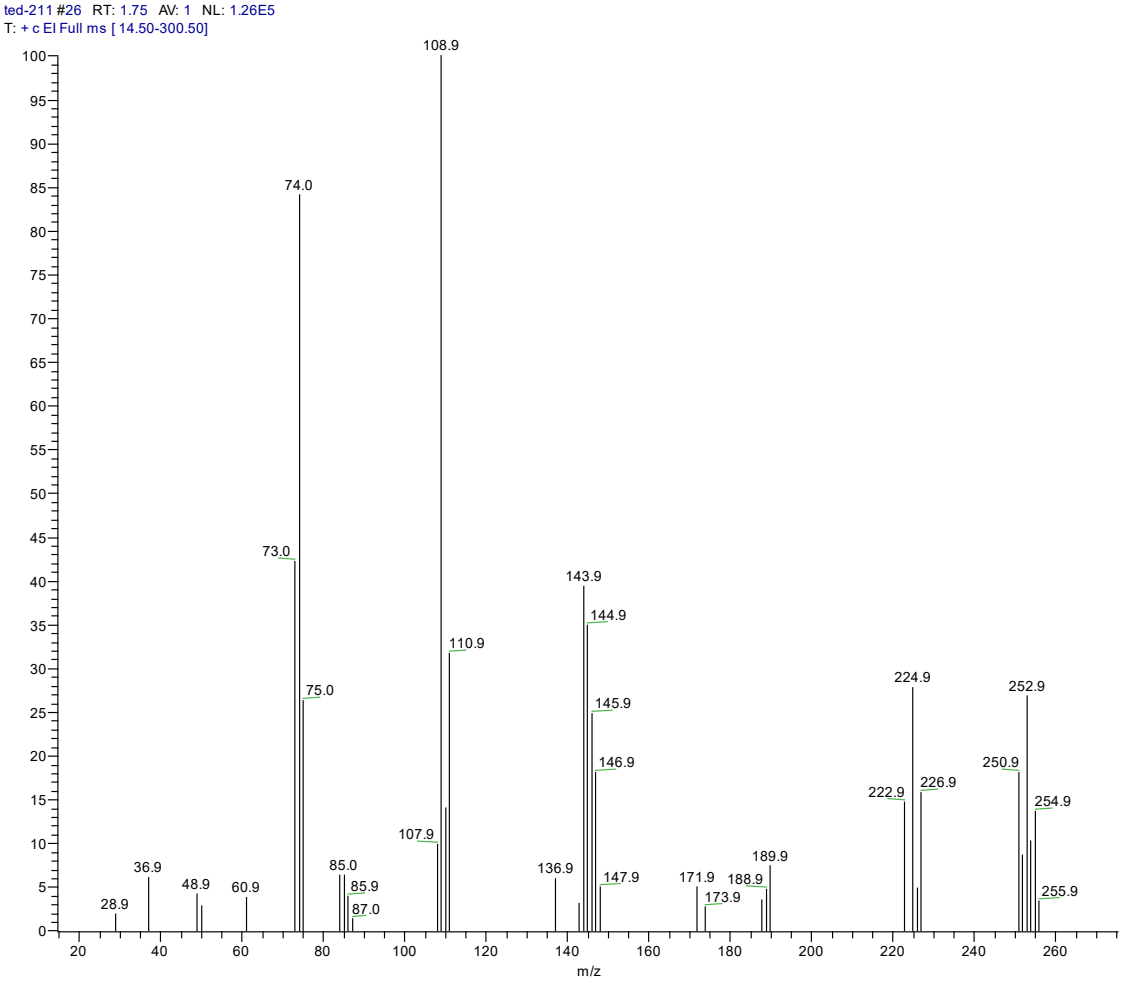

Figure S8. HRMS spectrum of 4-bromo-2,6-dichlorobenzaldehyde (**2**) (T_{source}=50 ˚C).

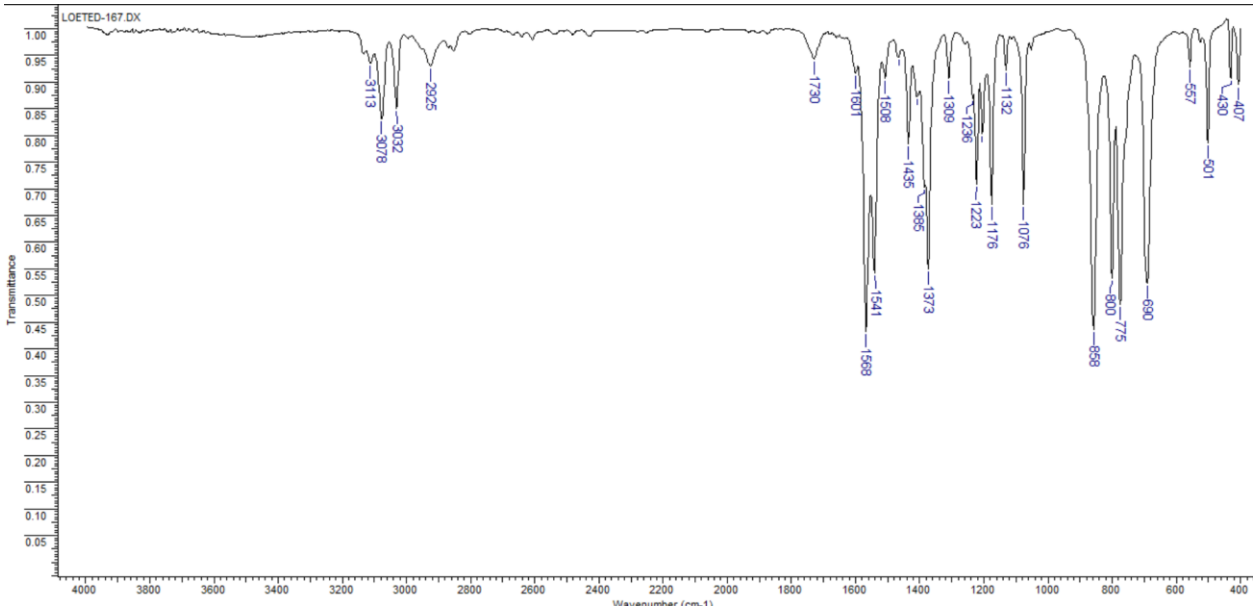

Figure S9. IR spectrum of 5-bromo-1,3-dichloro-2-(dichloromethyl)benzene (**3**) in KBr pellets.

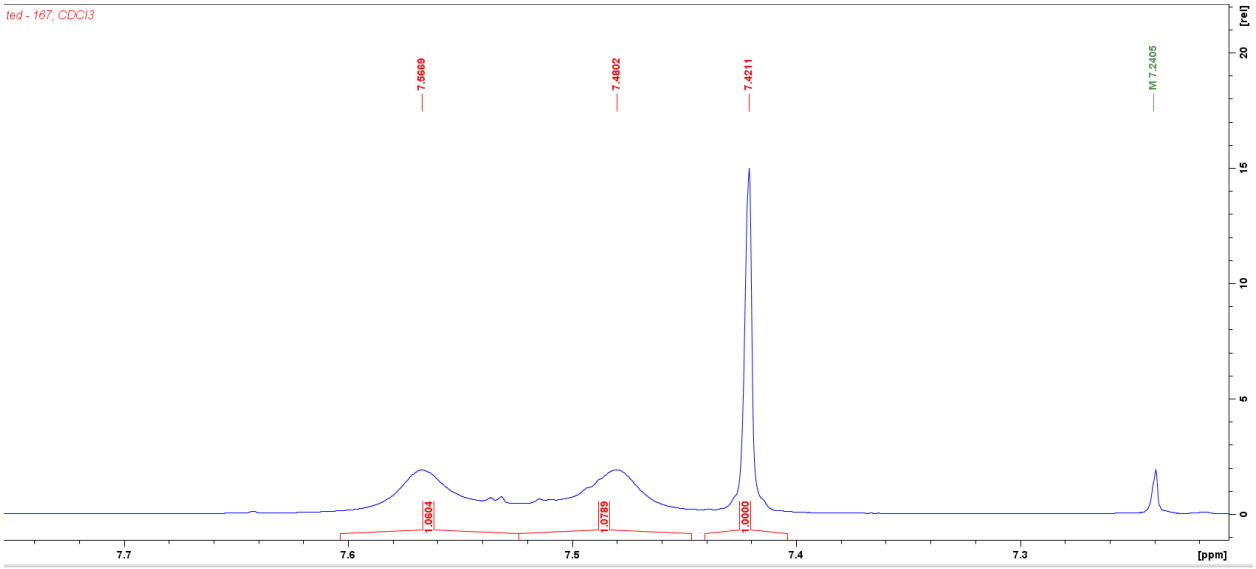

Figure S10. ^{1}H NMR spectrum of 5-bromo-1,3-dichloro-2-(dichloromethyl)benzene (**3**) in $CDCl_3$.

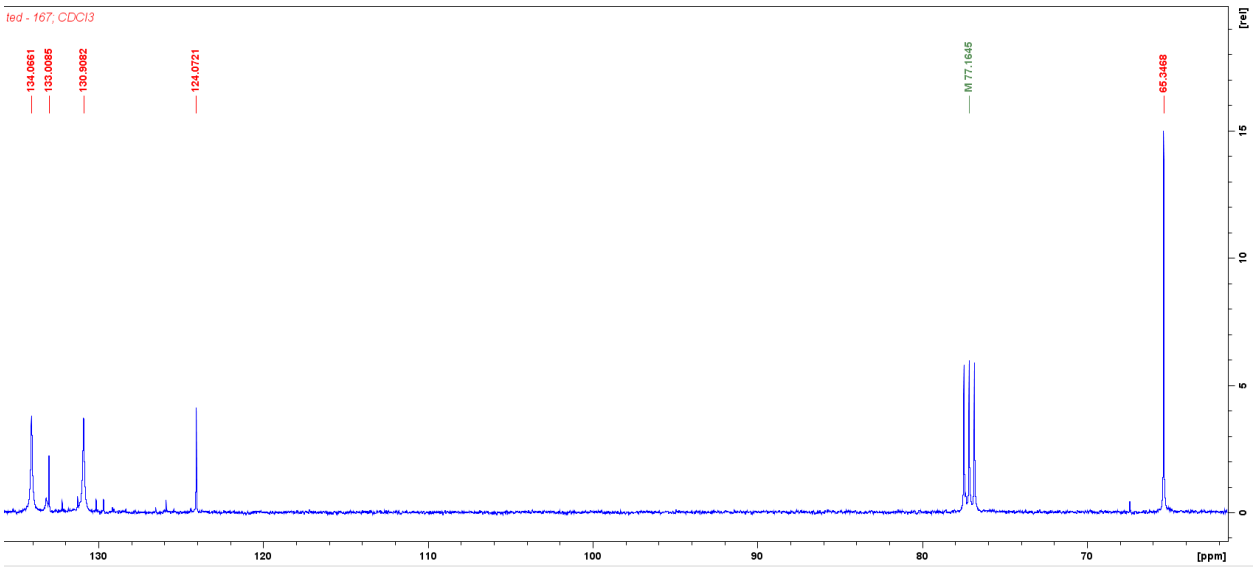

Figure S11. ^{13}C NMR spectrum of 5-bromo-1,3-dichloro-2-(dichloromethyl)benzene (**3**) in $CDCl_3$.

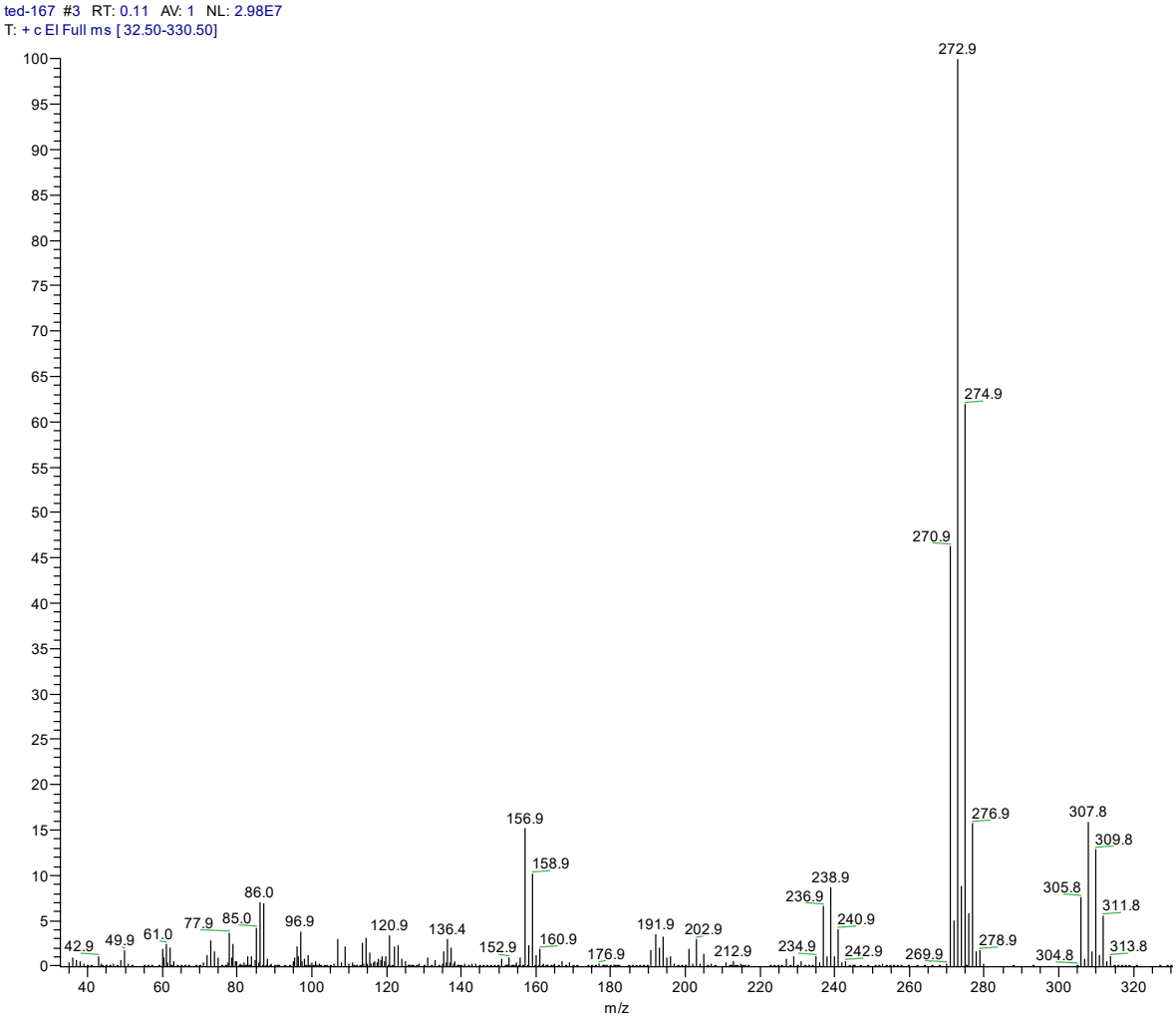

Figure S12. HRMS spectrum of 5-bromo-1,3-dichloro-2-(dichloromethyl)benzene (**3**) (T_{source}=50 ˚C).

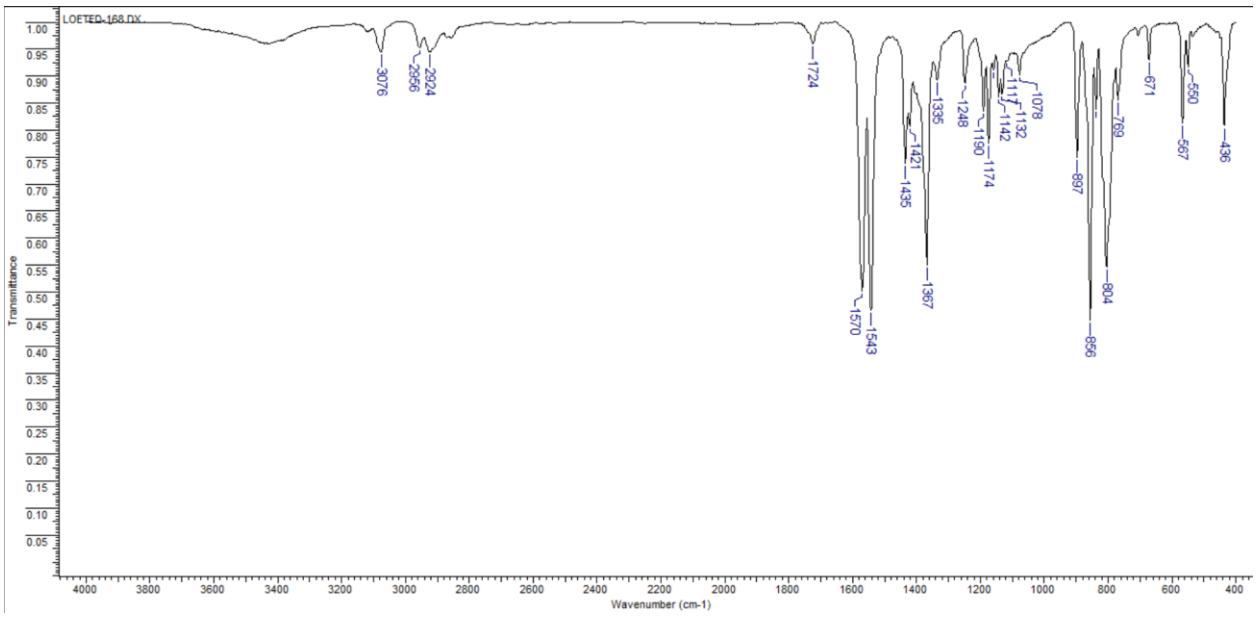

Figure S13. IR spectrum of **HTTM-Br** in KBr pellets.

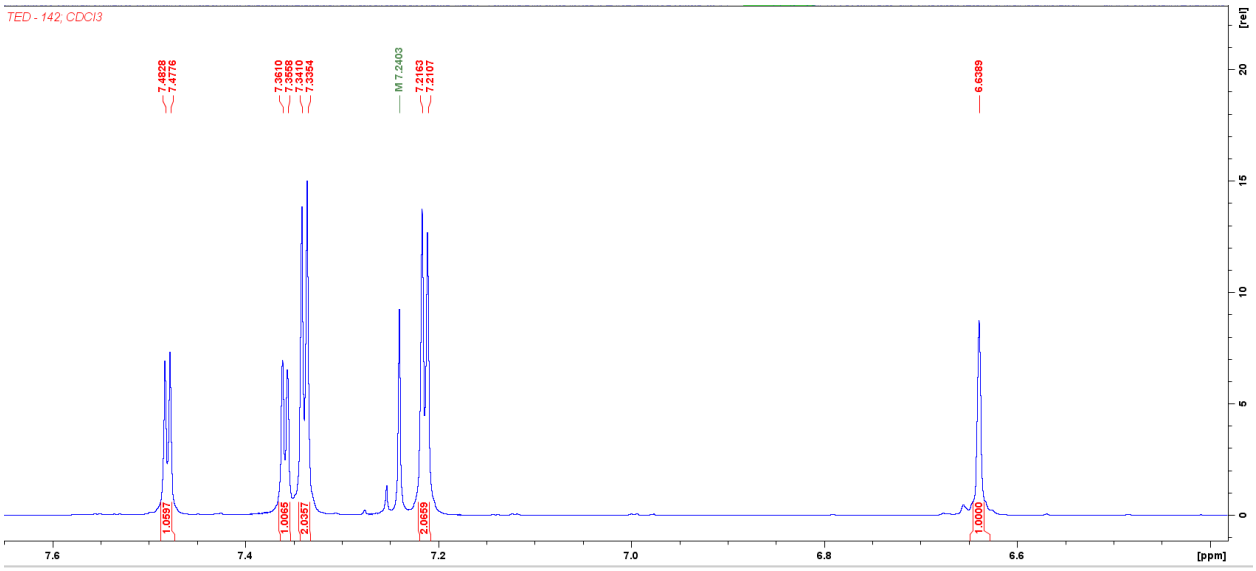

Figure S14. ^{1}H NMR spectrum of **HTTM-Br** in $CDCl_3$.

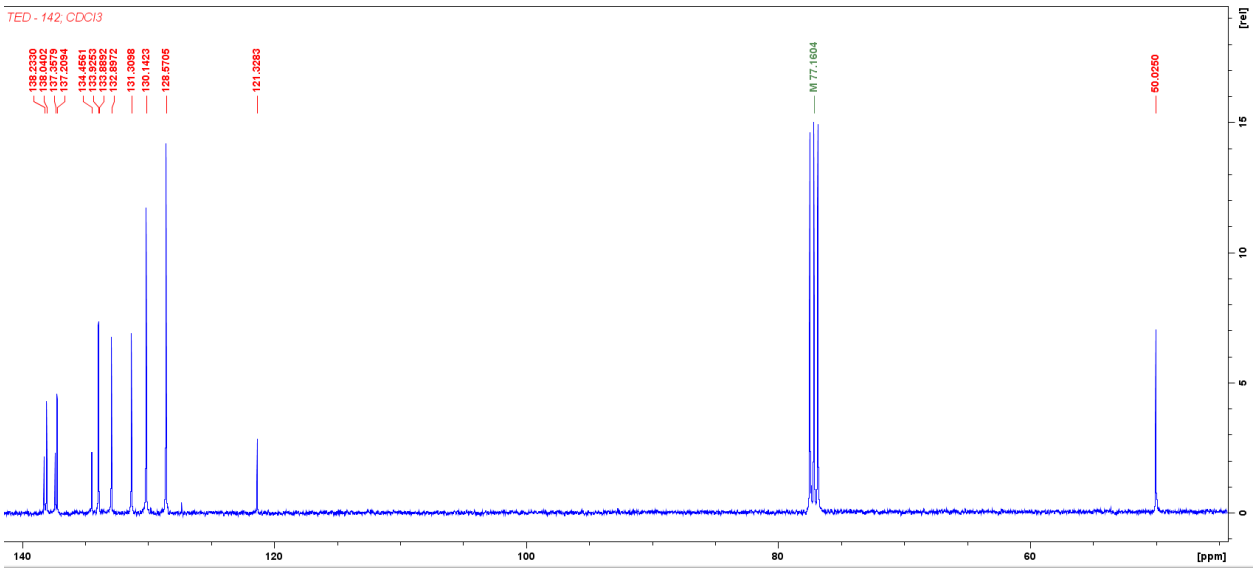

Figure S15. ^{13}C NMR spectrum of **HTTM-Br** in $CDCl_3$.

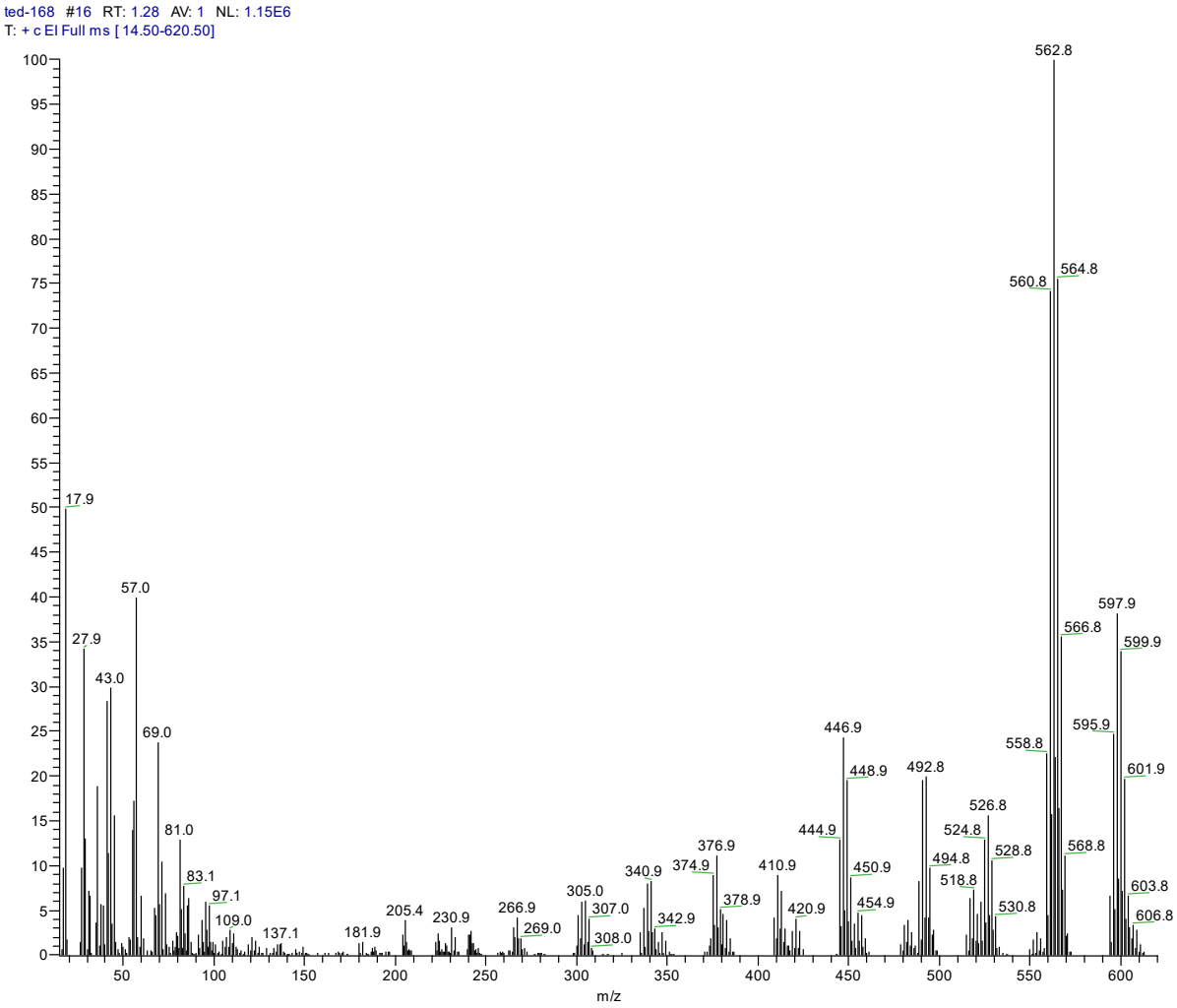

Figure S16. HRMS spectrum of **HTTM-Br** (T_{source}=100 ˚C, T_{probe}=250 ˚C).

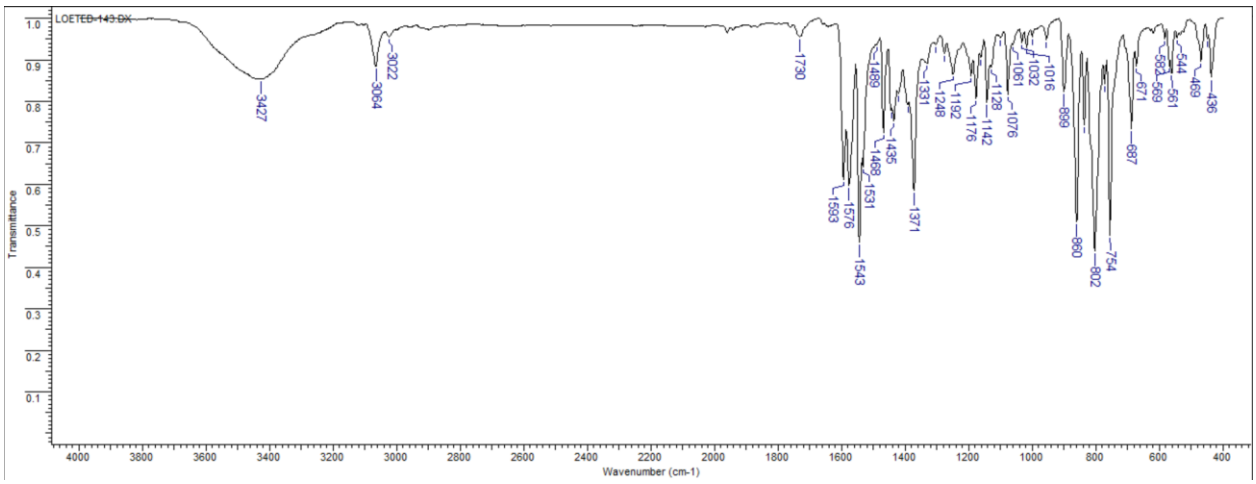

Figure S17. IR spectrum of **HTTM-TP** in KBr pellets.

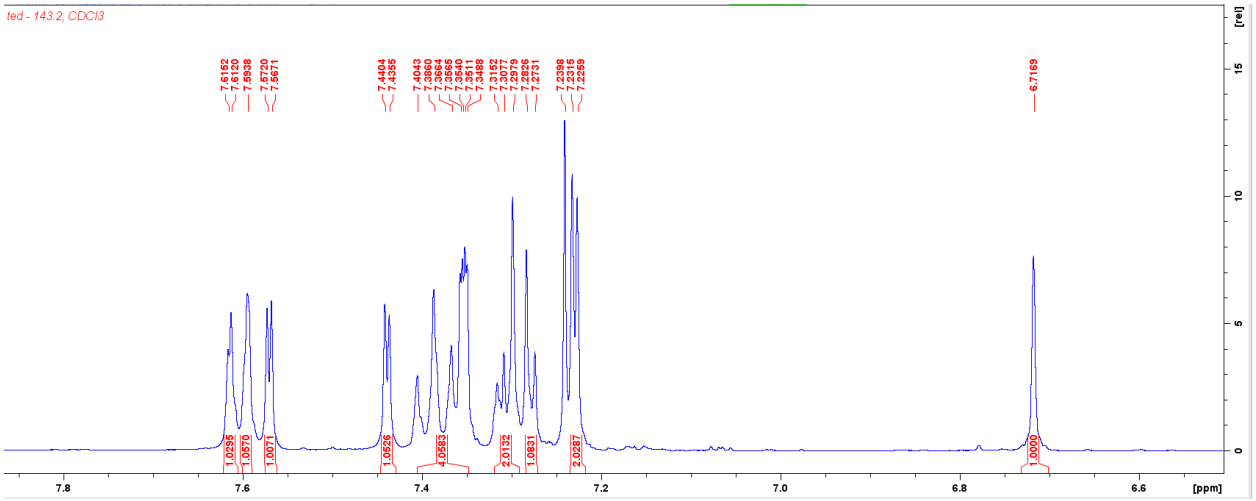

Figure S18. ^{1}H NMR spectrum of **HTTM-TP** in $CDCl_3$.

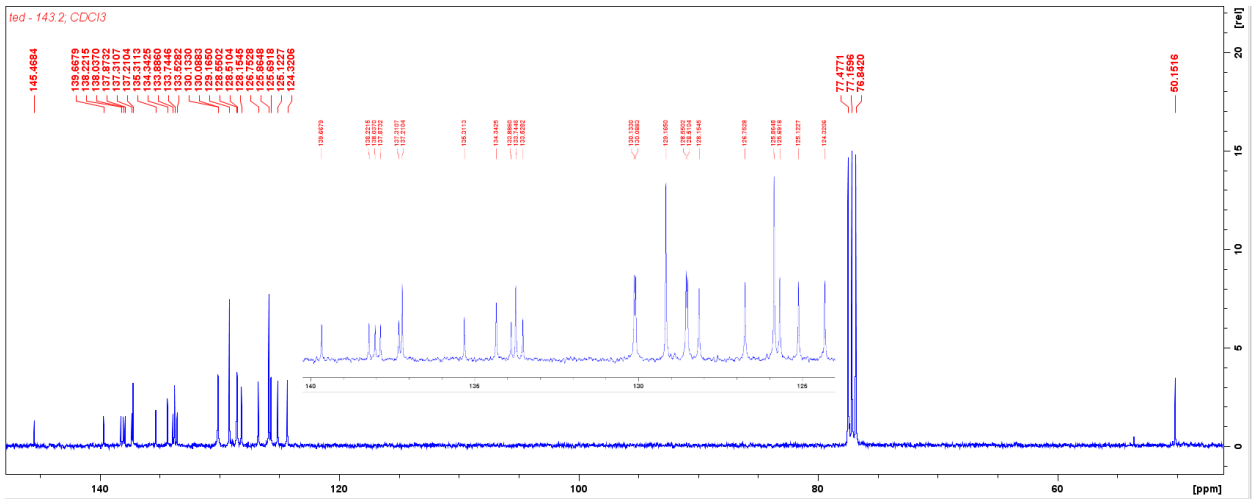

Figure S19. ^{13}C NMR spectrum of **HTTM-TP** in $CDCl_3$.

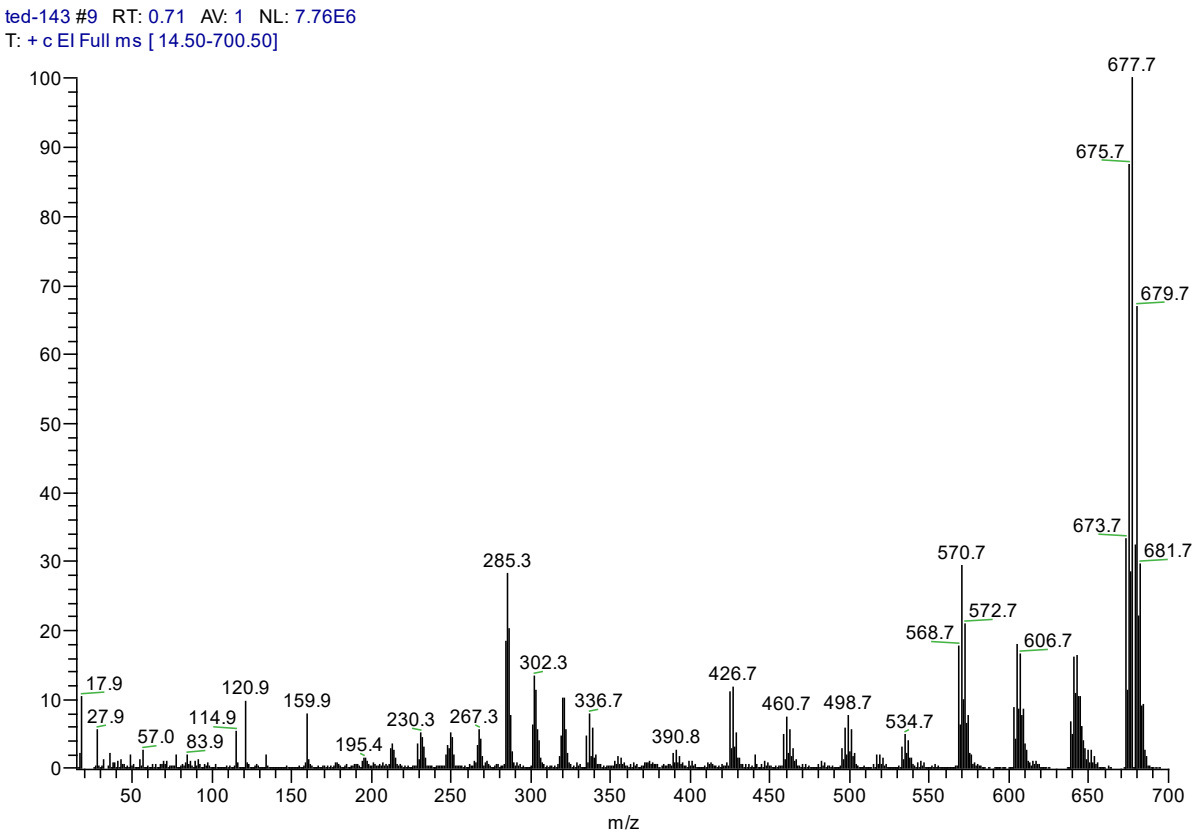

Figure S20. HRMS spectrum of **HTTM-TP** (T_{source}=130 ˚C, T_{probe}=240 ˚C).

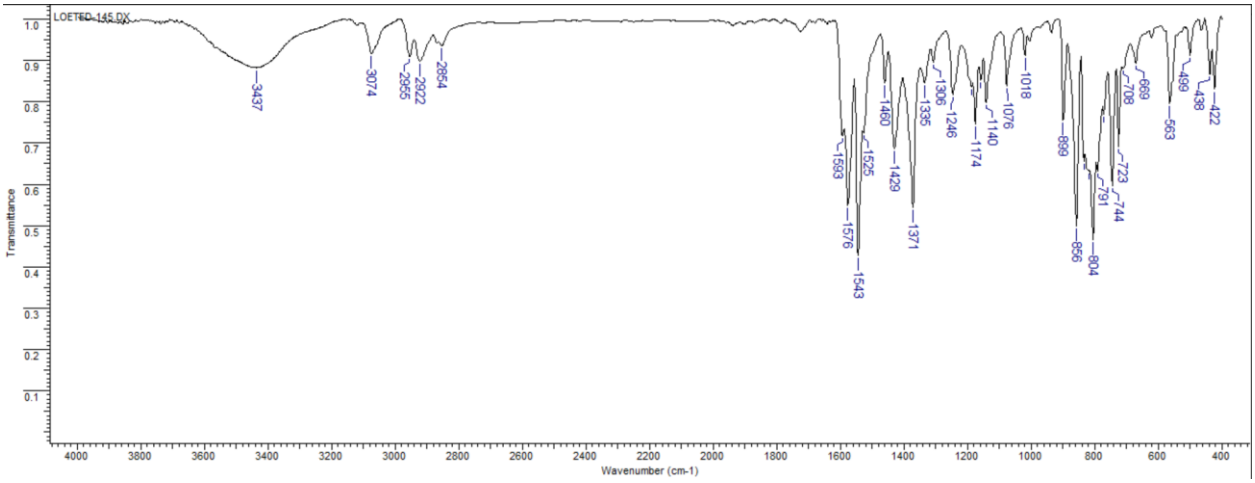

Figure S21. IR spectrum of **HTTM-BT** in KBr pellets.

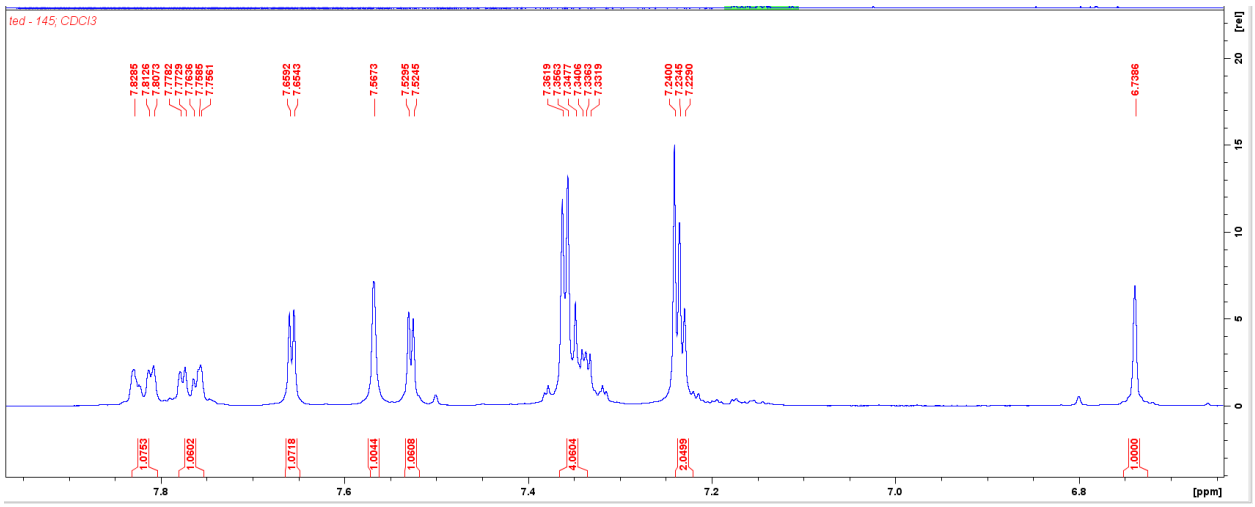

Figure S22. ^{1}H NMR spectrum of **HTTM-BT** in $CDCl_3$.

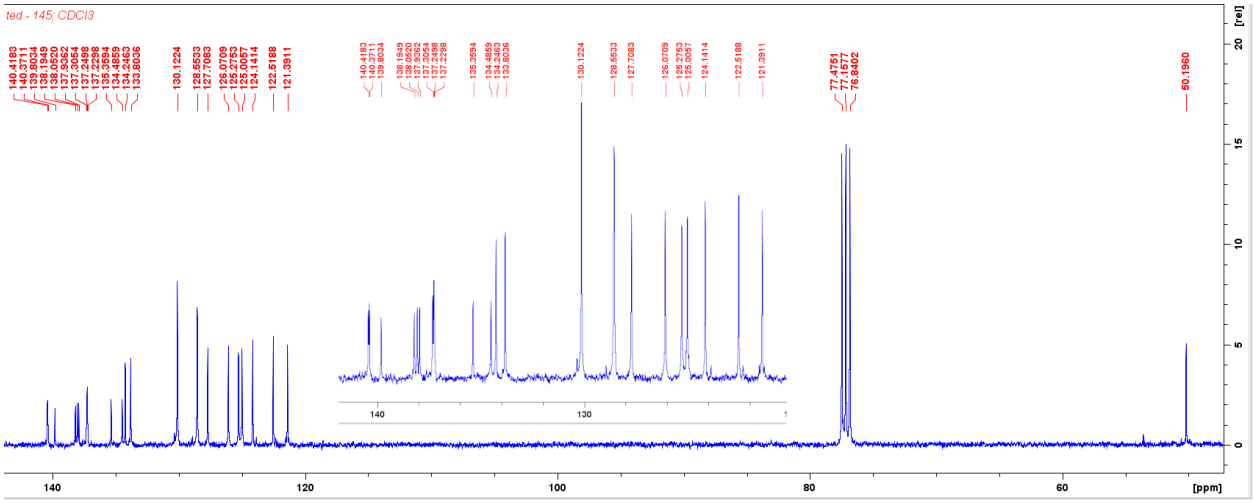

Figure S23. ^{13}C NMR spectrum of **HTTM-BT** in $CDCl_3$.

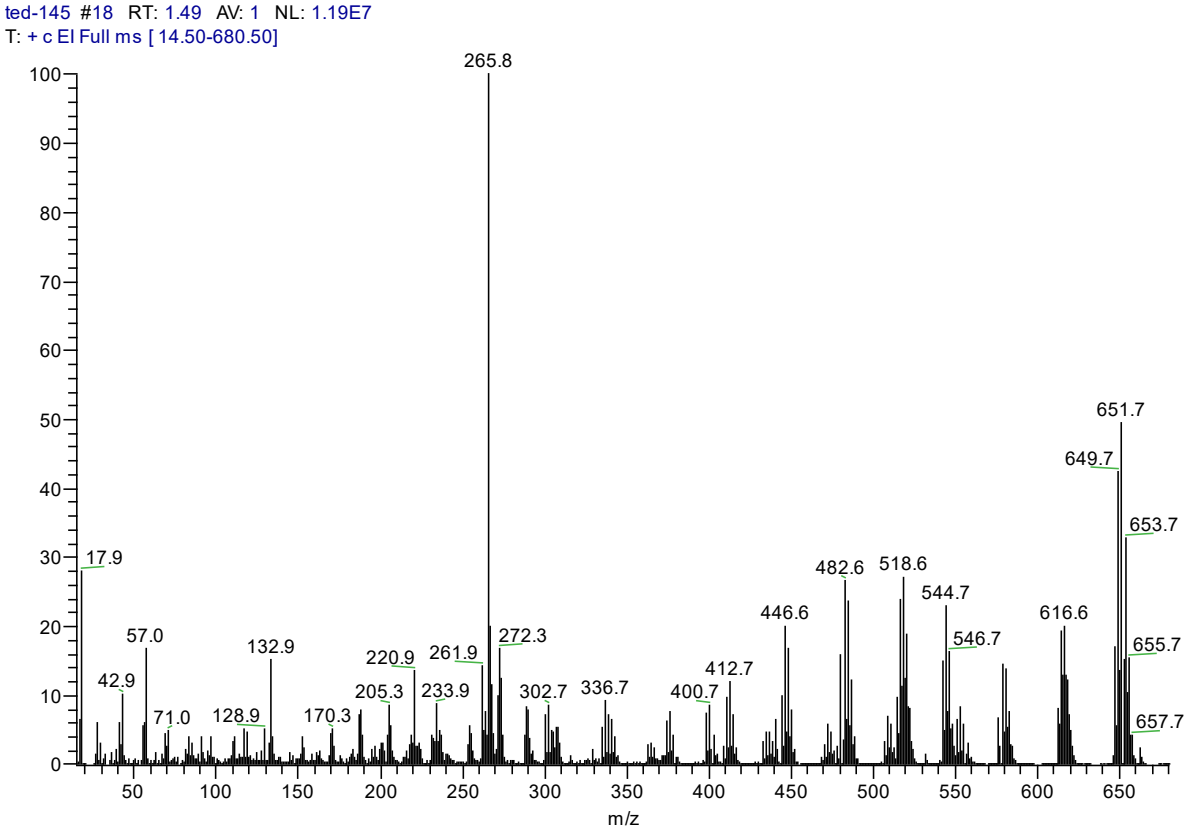

Figure S24. HRMS spectrum of **HTTM-BT** (T_{source}=135 ˚C, T_{probe}=240 ˚C).

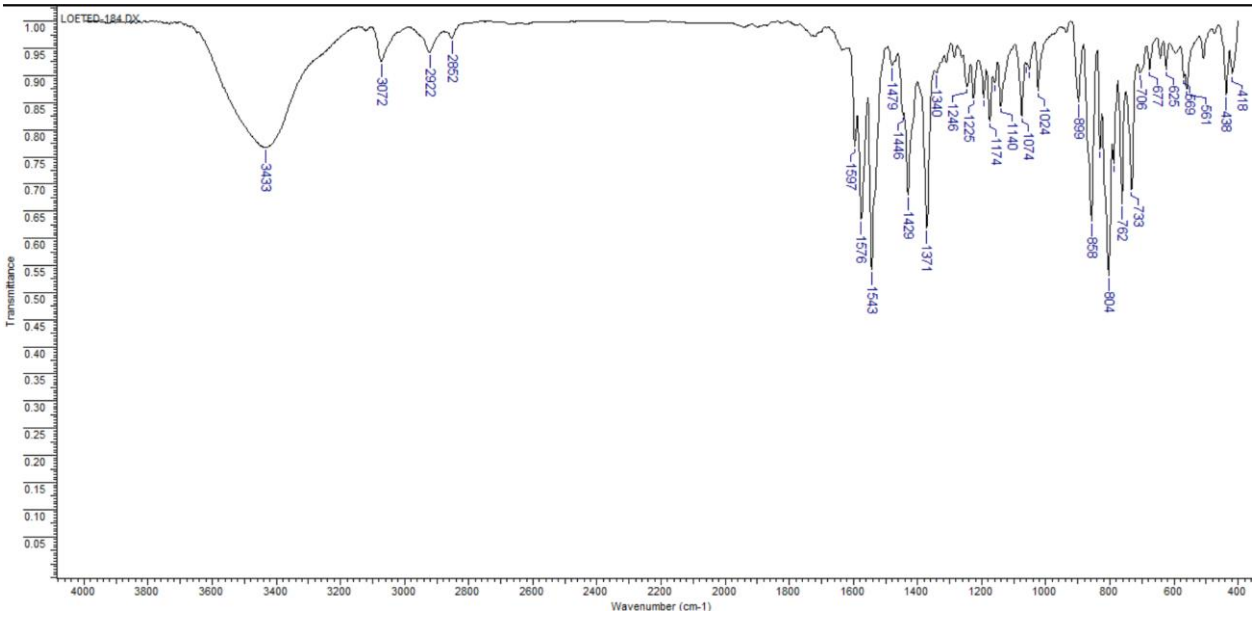

Figure S25. IR spectrum of **HTTM-DBT** in KBr pellets.

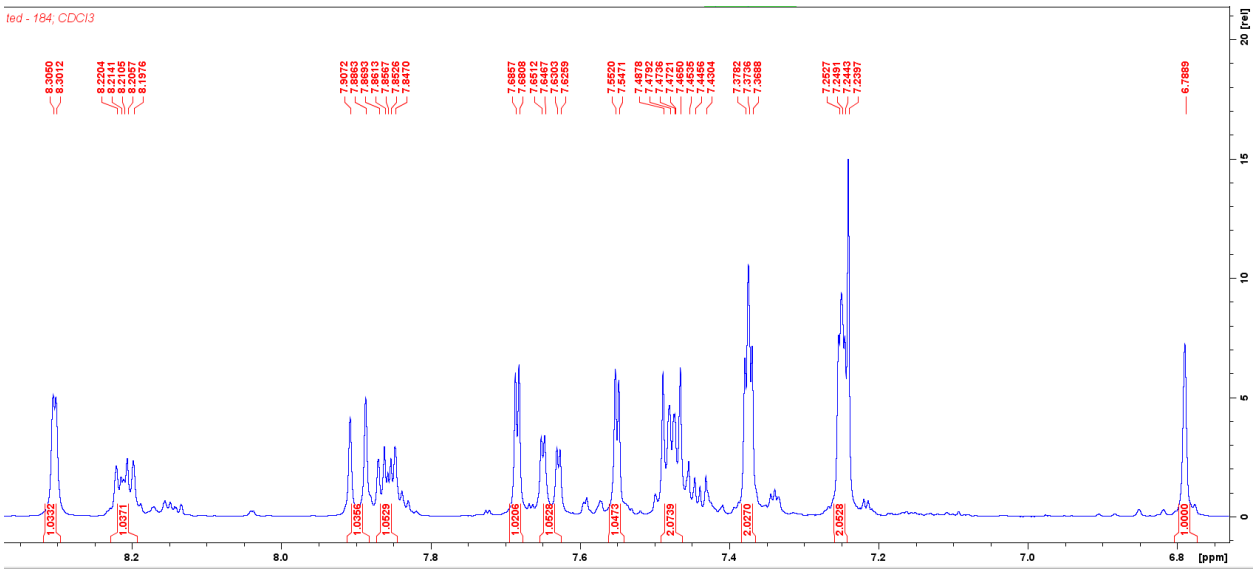

Figure S26. ^{1}H NMR spectrum of **HTTM-DBT** in $CDCl_3$.

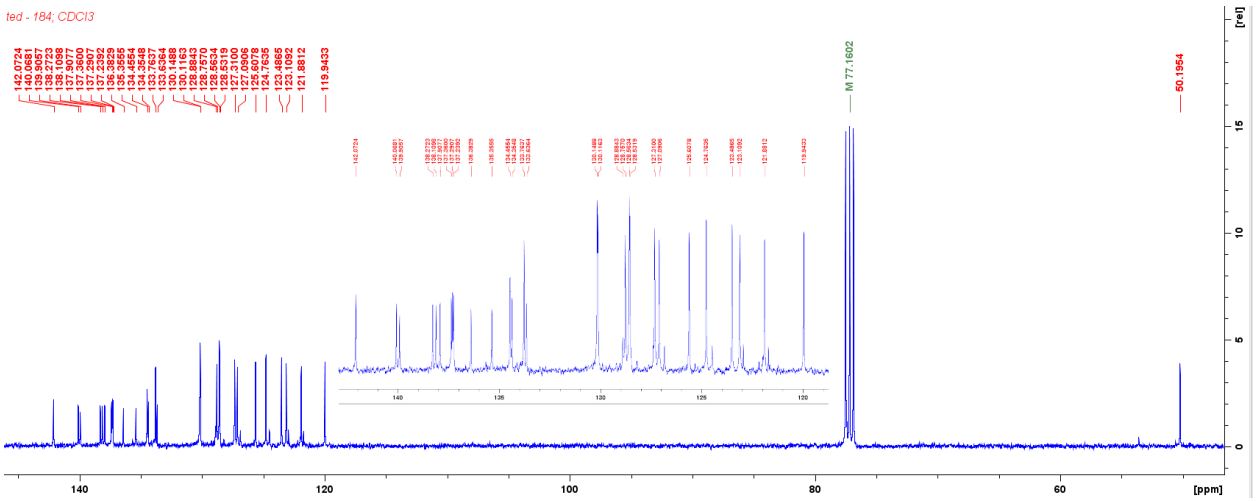

Figure S27. ^{13}C NMR spectrum of **HTTM-DBT** in $CDCl_3$.

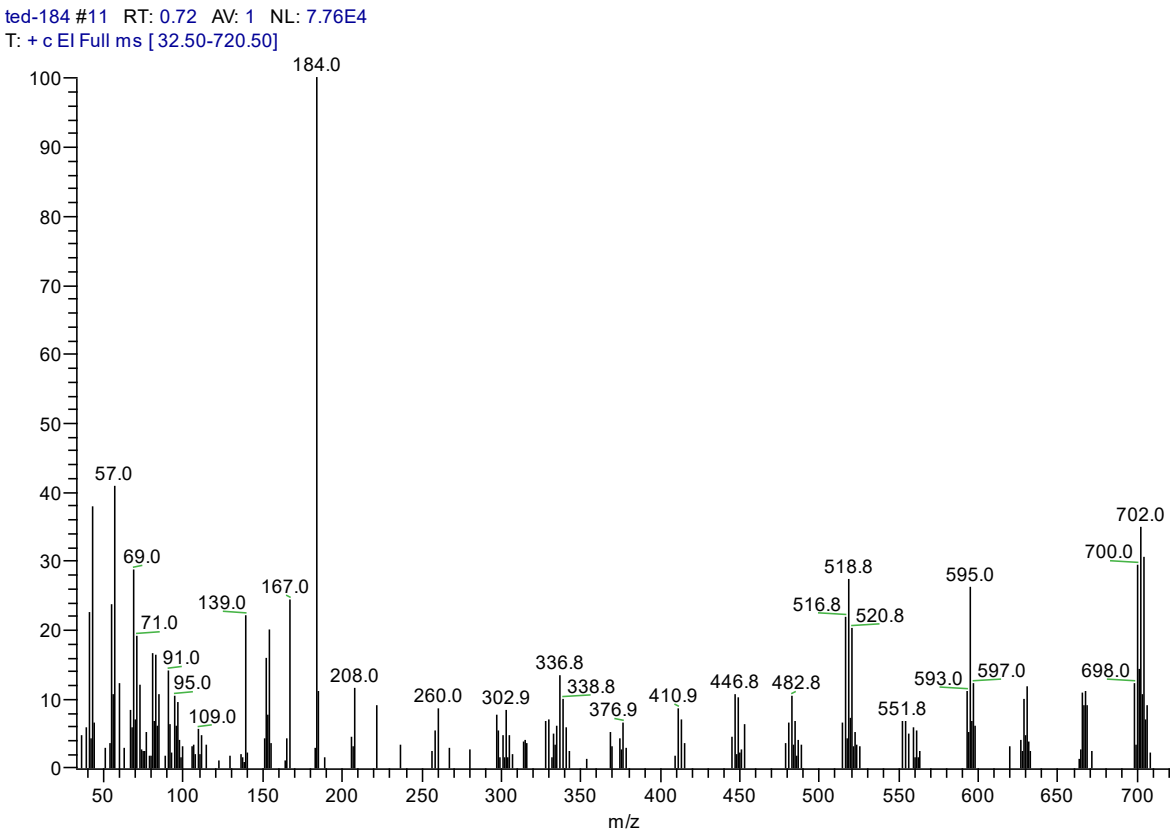

Figure S28. HRMS spectrum of **HTTM-DBT** (T_{source}=145 ˚C, T_{probe}=220 ˚C).

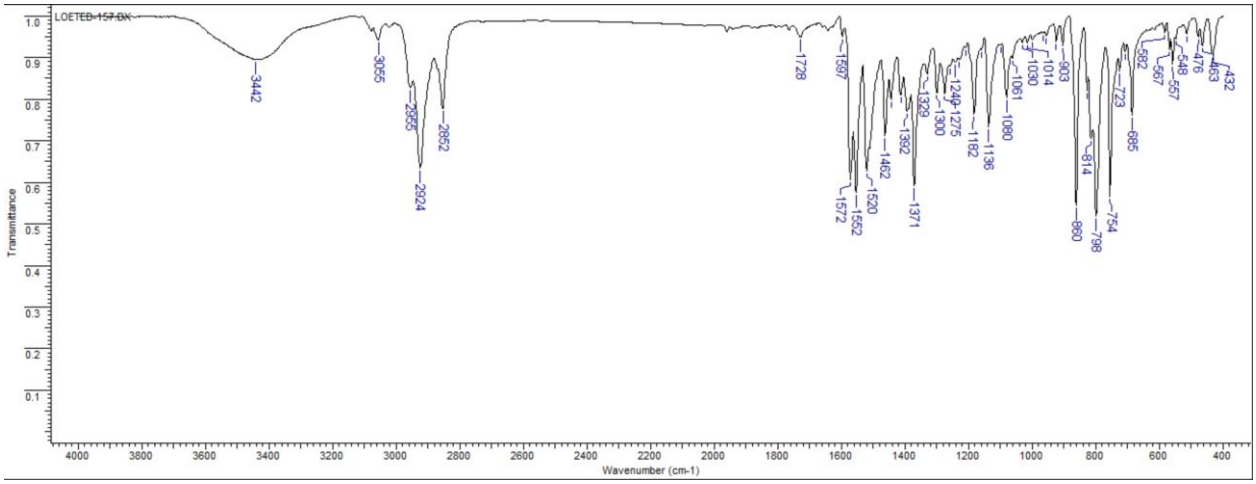

Figure S29. IR spectrum of **TTM-TP** in KBr pellets.

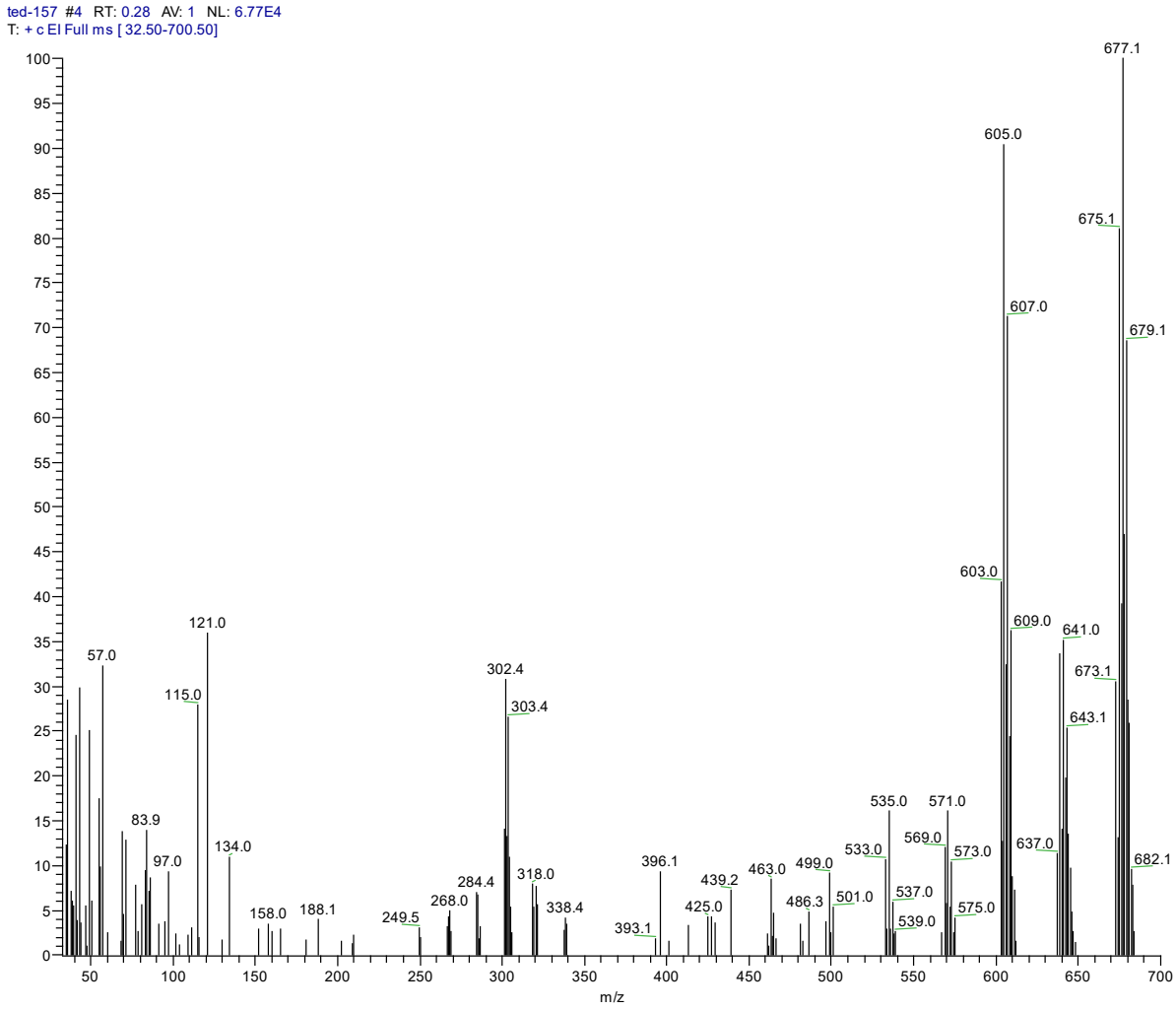

Figure S30. HRMS spectrum of **TTM-TP** (T_{source}=100 ˚C, T_{probe}=250 ˚C).

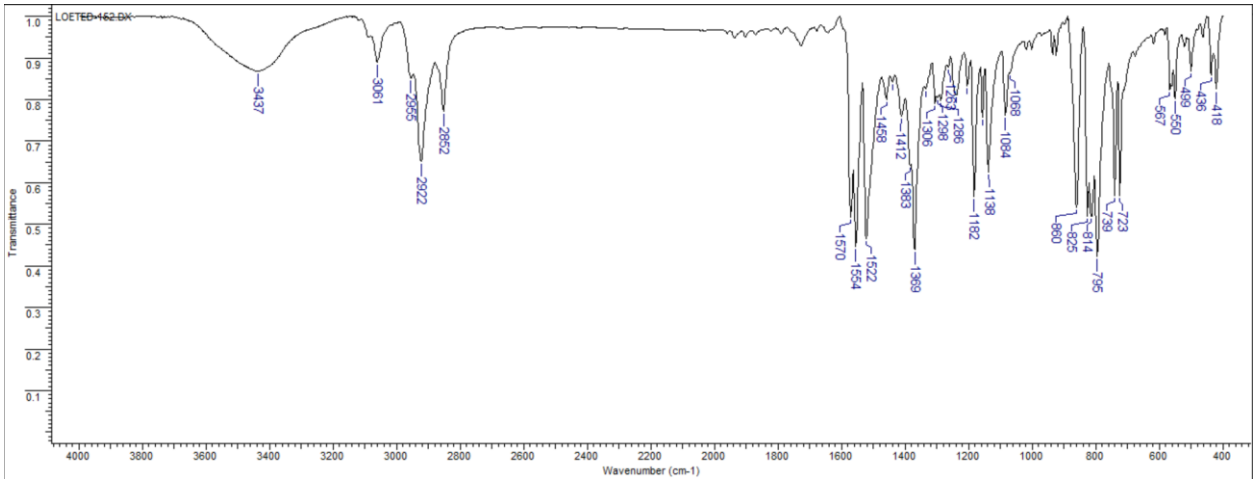

Figure S31. IR spectrum of **TTM-BT** in KBr pellets.

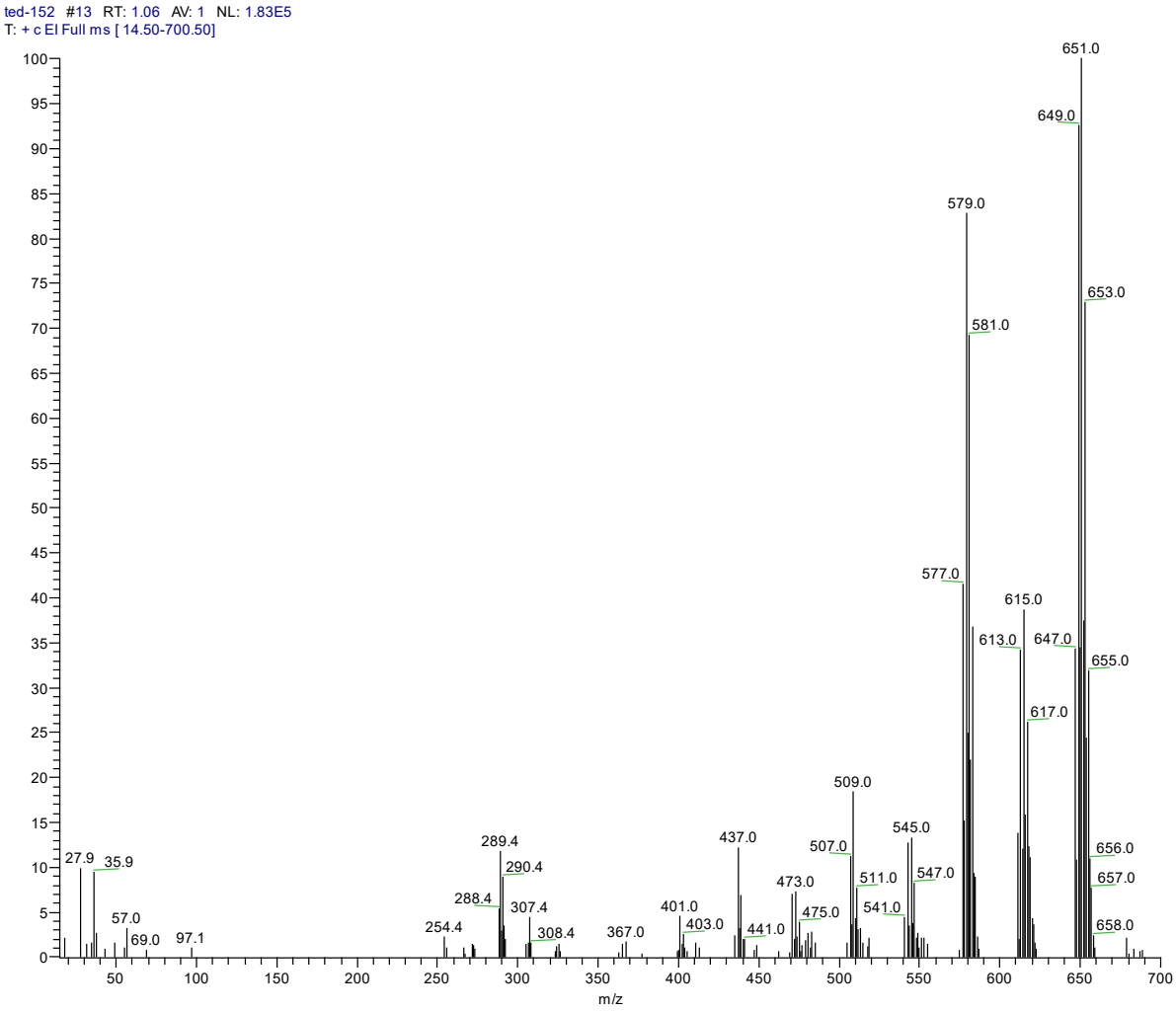

Figure S32. HRMS spectrum of **TTM-BT** (T_{source}=145 ˚C, T_{probe}=220 ˚C).

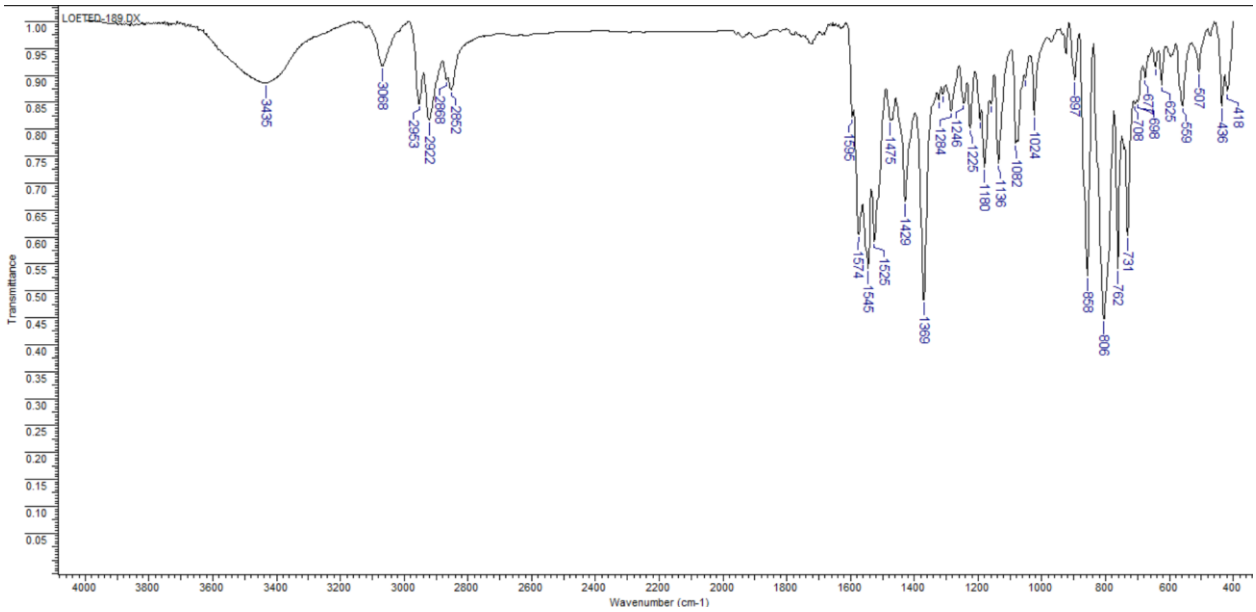

Figure S33. IR spectrum of **TTM-DBT** in KBr pellets.

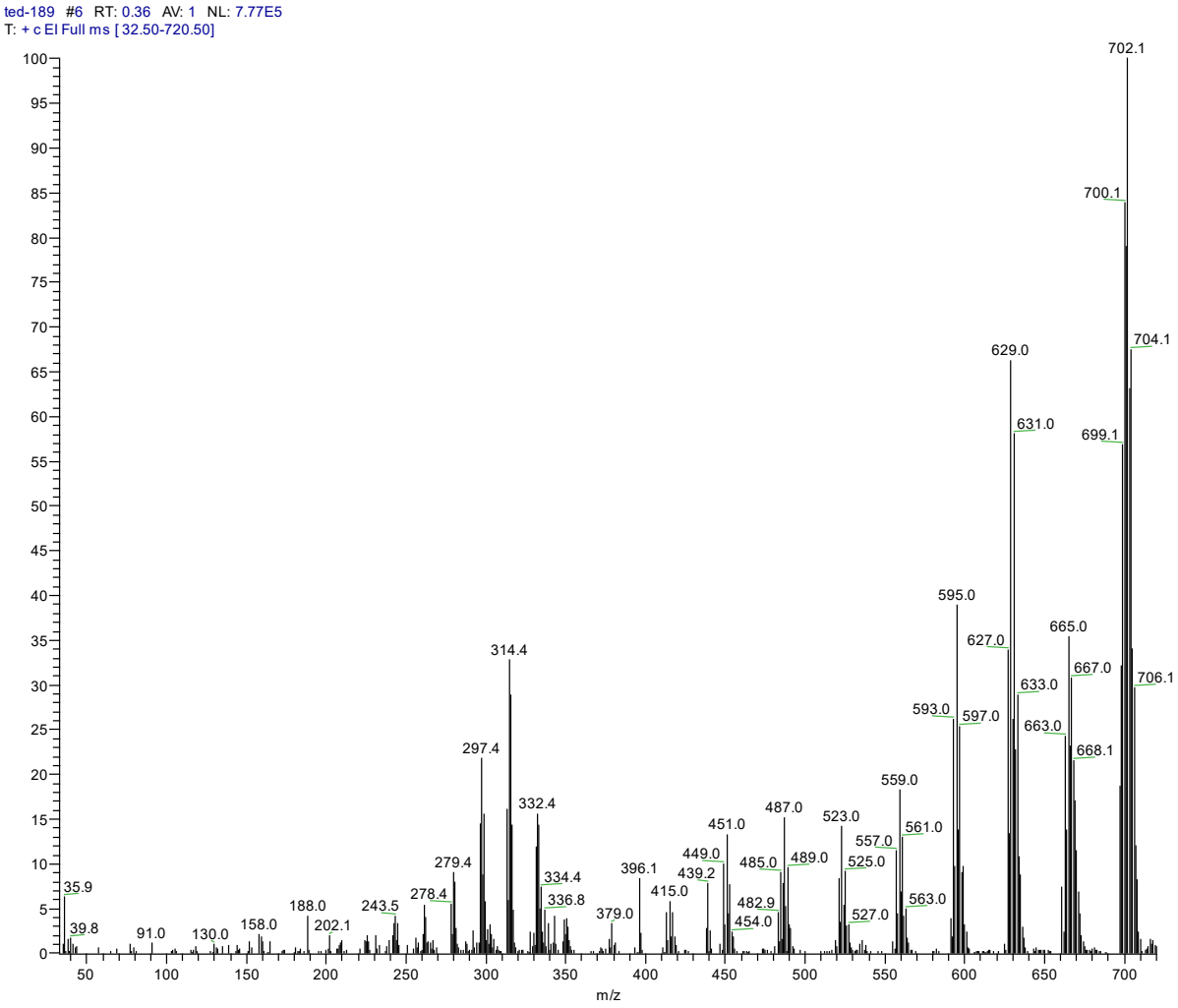

Figure S34. HRMS spectrum of **TTM-DBT** (T_{source}=100 ˚C, T_{probe}=300 ˚C).

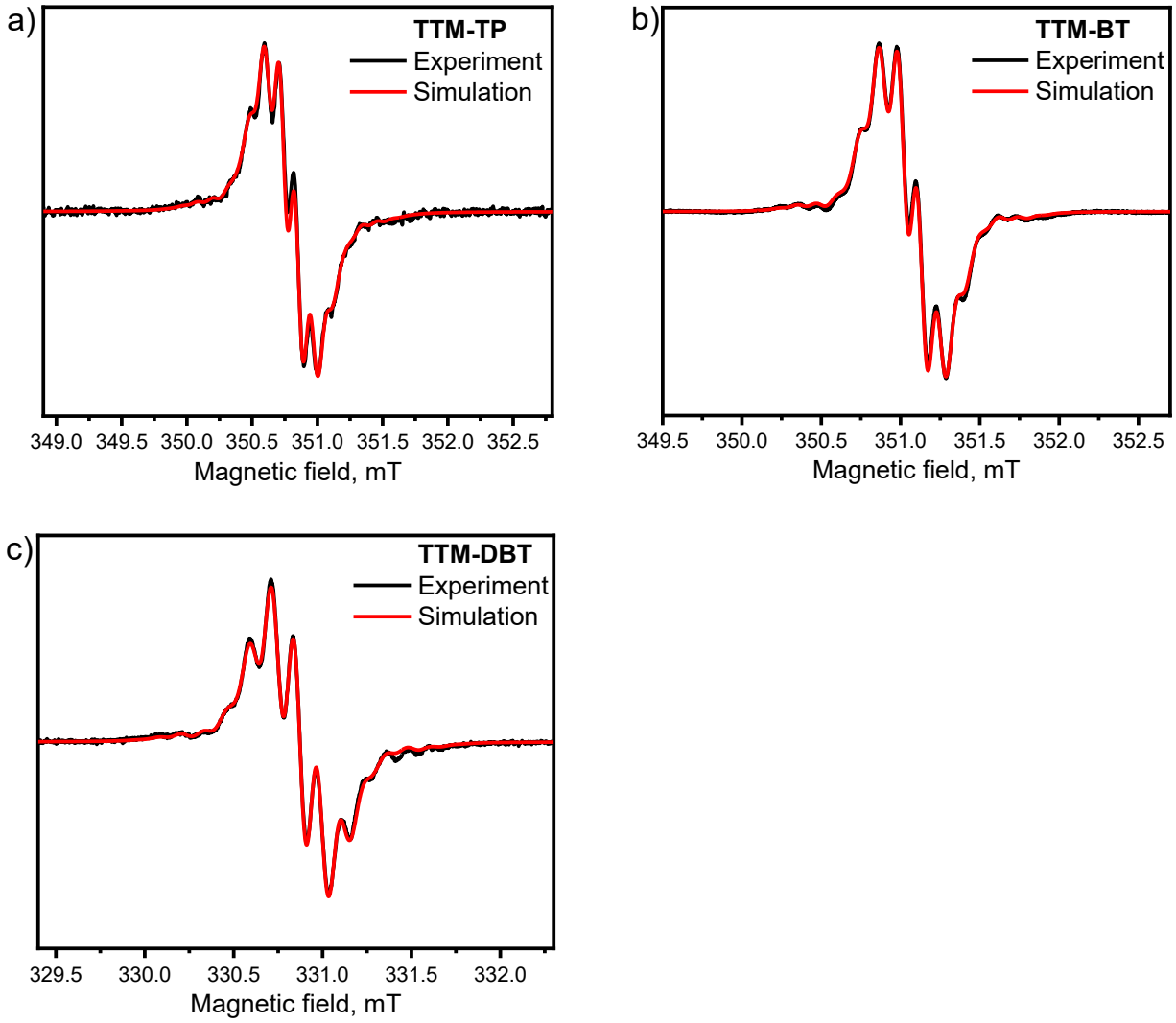

Figure S35. Room temperature EPR spectra of **TTM-TP** (a), **TTM-BT** (b), **TTM-DBT** (c), in deoxygenated DMSO solutions C=10^{-4} M. Experimental spectra marked by black line, simulated – by red. The spectra contain satellites due to ^{13}C isotopes.

Table S3. EPR spectra simulation parameters for 10^{-4} M DMSO solutions of radicals.

	g-factor	Line width, mT	$a_{H\gamma}$, mT	$a_{^{13}C}$, mT
TTM-TP	2.01118	0.017	0.115	1.03
TTM-BT	2.00943	0.013	0.116	1.03
TTM-DBT	2.0102	0.0055	0.122	1.02

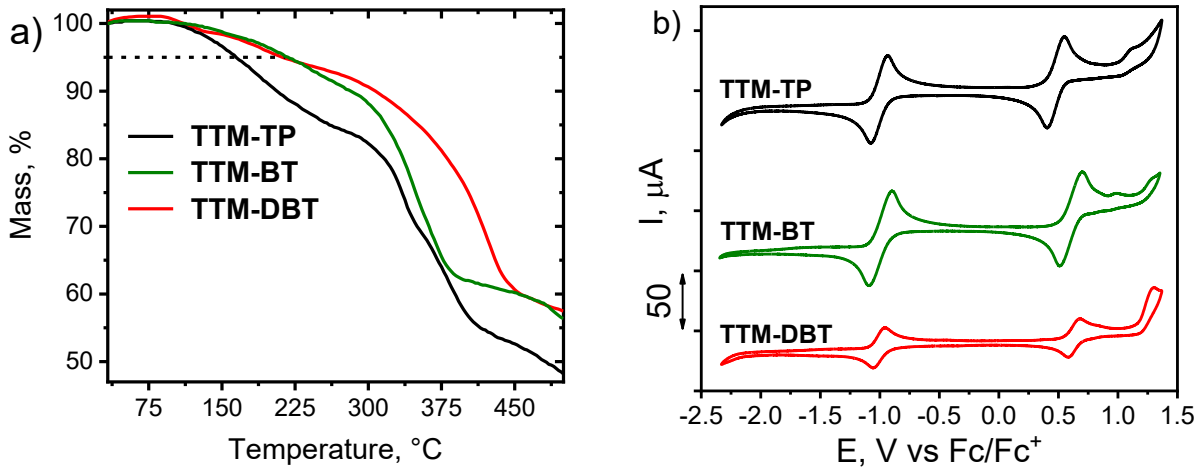

Figure S36. Thermal gravimetric analysis for studied compounds in helium atmosphere: **TTM-TP** (black), **TTM-BT** (olive) and **TTM-DBT** (red) (a); cyclic voltammograms of studied radicals in CH_2Cl_2 solution (b).

Table S4. Summarized electronic and thermal properties for radicals. E_{ox} and E_{Red} are the half-wave oxidation and reduction potentials respectively. E_{SOMO} and E_{SUMO} were calculated from the oxidation and reduction half-wave potentials, respectively. E_g was calculated from the blue edge of PL spectra. $T_{5\%}$ is 5% weight-loss temperature.

Radical	E_{Ox}, V *vs* Fc/Fc^+	E_{Red}, V *vs* Fc/Fc^+	E_{SOMO}, eV	E_{SUMO}, eV	E_g, eV	E_{HOMO}, eV	$T_{5\%}$, °C
TTM-TP	0.48	–1.00	–5.28	–3.80	1.69	–5.49	165
TTM-BT	0.61	–1.00	–5.41	–3.80	1.78	–5.58	218
TTM-DBT	0.63	–1.00	–5.43	–3.80	1.97	–5.77	208

4. X-ray data

Supplementary Note S2. Crystal structure of TTM-derivatives

TTM-TP and **TTM-DBT** have a similar crystal packing, specifically a layered structure with head-to-head molecular arrangement with Cl···Cl interactions (Fig. S37) which can be attributed to the σ-hole halogen bonding due to the II type of interactions where C-Cl···Cl (θ1) and Cl···Cl-C (θ2) angles are close to 180° and 90°, respectively. The distances between the chlorine atoms are less than the sum of the van der Waals radii according to Bondi (<3.5 Å). **TTM-TP** and **TTM-DBT** have a similar substituent inclination within the layers (relative to the (100) plane, Fig. S37b, h). Cl···Cl contacts between TTM fragments in **TTM-TP** additionally stabilized by C–H···π interactions between TTM and TP fragments (Fig. S37a). The chains of molecules in **TTM-TP** are linked *via* Cl···Cl and C–H···Cl interactions between TTM and substituent fragments (Fig. S37g, h), whereas in **TTM-DBT** C–Cl···π and Cl···S interactions are additionally formed due to the extensive π-system. The structure of **TTM-BT** differs significantly from the two described above. The compound crystallizes in green plates (Fig. S37a). The conformation of **TTM-BT** ($\varphi_{4/4A}$ angle) is non-planar, but intramolecular C-H···S interactions also form (Fig. S37, Table S7). The **TTM-BT** molecules have the highest tilt in respect to (100) plane due to which a herringbone packing is formed inside the layers (Fig. S37b). The herringbone packing is formed by numerous C-H···π, C-Cl···π and C-H···Cl interactions between TTM and benzothiophene fragments (Fig. S37, Table S7).

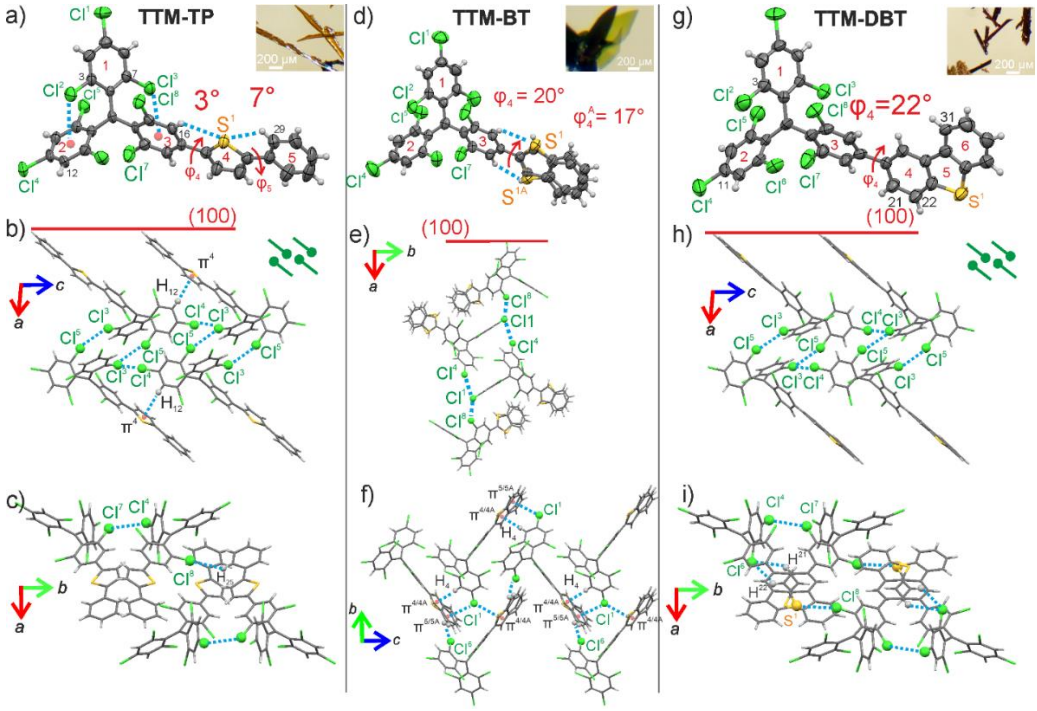

Figure S37. Molecular structure with atomic numbering, torsion angles and optical image of **TTM-TP, TTM-BT** and **TTM-DBT** (a, d, g); chains of Cl···Cl interactions along the c-axis and the head-to-head packing (b, e, h); intralayer interactions along the *b*-axis (c, f, i).

Table S5. Crystal data, data collection, and structure refinement parameters for **TTM-TP**, **TTM-BT** and **TTM-DBT** at 296 K.

	TTM-TP	**TTM-BT**	**TTM-DBT**
	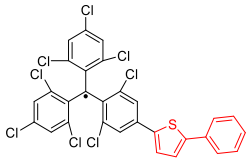	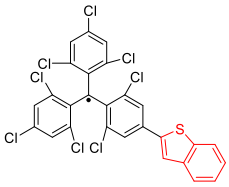	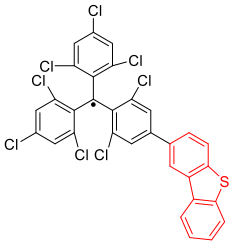
Chemical formula	$C_{29}H_{13}Cl_8S$	$C_{27}H_{11}Cl_8S$	$C_{31}H_{13}Cl_8S$
M_r	677.05	651.02	701.07
Crystal system, space group	Monoclinic, $P2_1/c$		
a, b, c (Å)	14.594 (5) 18.111 (5) 10.613 (3)	14.414 (4) 12.147 (3) 15.983 (3)	14.8323 (17) 19.2071 (18) 10.2458 (11)
β (°)	95.466 (15)	102.618 (11)	96.385 (5)
V (Å^3)	2792.3 (15)	2730.8 (11)	2900.8 (5)
Z/Z'	4/1		
D_{calcd} (g cm^{-3})	1.611	1.584	1.605
No. of measured, independent and observed [$I > 2\sigma(I)$] reflections	17720, 4927, 2319	17210, 4819, 2057	19114, 5112, 1776
R_{int}	0.124	0.082	0.154
$R[F^2 > 2\sigma(F^2)]$, $wR(F^2)$, S	0.085, 0.239, 1.04	0.053, 0.134, 1.01	0.068, 0.155, 0.94
$\Delta\rho_{max}$, $\Delta\rho_{min}$ (e Å^{-3})	0.40, −0.46	0.32, −0.37	0.23, −0.38

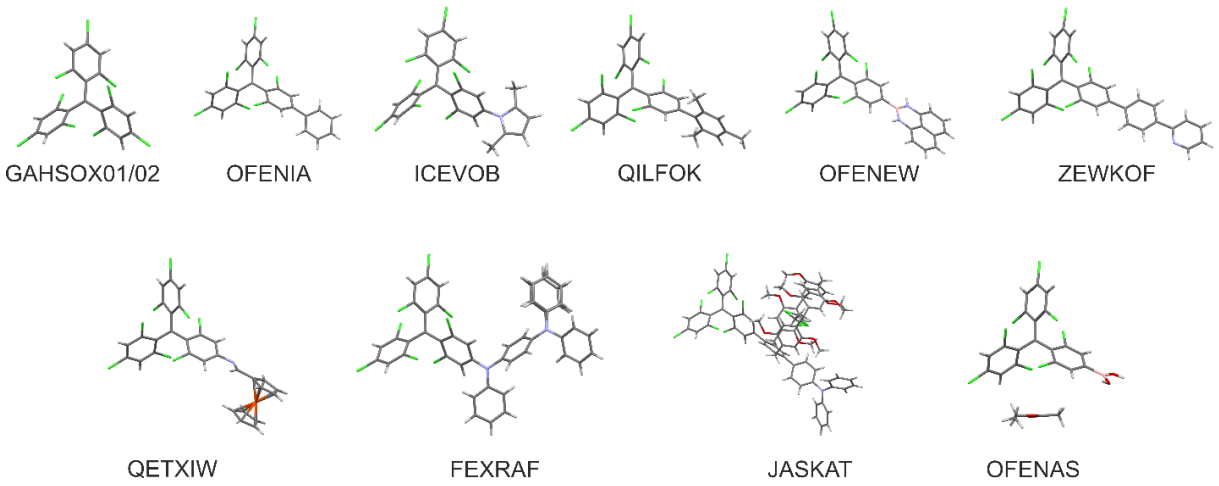

Figure S38. A few reported derivatives of the TTM radical from the Cambridge Structural Database with the corresponding refcodes.

Table S6. The torsion angle values of the TTM fragment structures taken from CSD in comparison with the structures obtained in this work.

	Refcode	φ_1	φ_2	φ_3
1	GAHSOX01	46.4	47.1	46.4
2	FEXRAF	44.9(3)	47.8(3)	49.5(3)
3	ICEVOB	39.0(3)	54.7(3)	47.9(3)
4	JASKAT	40.6(5)	53.7(5)	44.5(5)
5	OFENAS	46.4(6)	52.1(6)	48.8(6)
6	OFENEW	48.3(4)	49.7(4)	48.1(4)
7	OFENIA	48.1(4)	51.7(4)	50.1(4)
8	QETXIW	45.4(8)	50.7(7)	49.0(8)
9	QILFOK	47.0	48.2	45.3
10	ZEWKOF	42.9(5)	54.0(5)	47.8(5)
11	**TTM-TP**	**43(1)**	**46(1)**	**49(1)**
12	**TTM-BT**	**44(4)**	**53(4)**	**47(4)**
13	**TTM-DBT**	**44(1)**	**50(1)**	**52(1)**

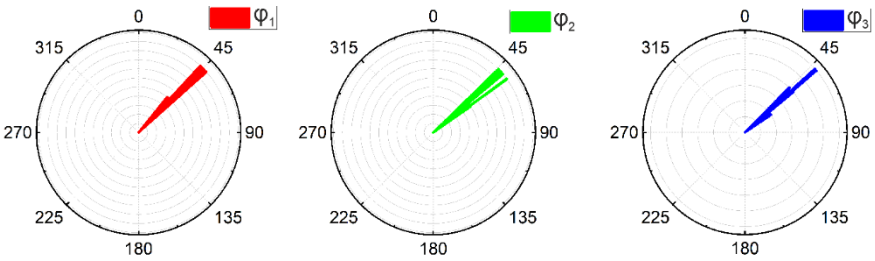

Figure S39. Angular distribution of torsion angles φ_1, φ_2, φ_3 in 14 previously reported – donor TTM derivatives according to CCDC.

Table S7. Noncovalent interactions in crystals of radicals at 296 K. Cg is the aromatic ring center; D_{pln} is the nearest distance between H-atom and aromatic ring plane. Label atoms correspond to the label scheme in Fig. S37.

		H···Cg (Å)	D_{pln} (Å)	C-H···Cg (°)
TTM-TP	C_{12}-H···π4	2.92	2.89	172
		Cl···Cg (Å)	D_{pln} (Å)	C-H···Cg (°)
	C_3-Cl_2··· π2 (intra)	3.465(4)	3.040	95.6(3)
	C_7-Cl_3··· π3 (intra)	3.392(4)	2.979	98.6(3)
		Cl···Cl (Å)	C-Cl···Cl (°)	Cl···C-Cl (°)
	Cl_3···Cl_4	3.371(3)	172.6(3)	117.6(3)
	Cl_7···Cl_4	3.393(4)	138.7(3)	90.3(3)
	Cl_3···Cl_5	3.407(3)	160.9(3)	112.7(3)
		H···A (Å)	D···A (Å)	D-H···A (°)
	C_{16}-H···S_1(intra)	2.68	3.079(8)	107
	C_{29}-H···S_1(intra)	2.70	3.099(10)	107
	C_{25}-H···Cl_8	3.034	3.82(1)	143.4
TTM-BT		H···Cg (Å)	D_{pln} (Å)	C-H···Cg (°)
	C_{10}-H···π4/4A	2.84/2.81	2.82/2.80	178/176
		Cl···Cg (Å)	D_{pln} (Å)	C-Cl···Cg (°)
	C_{11}-Cl_4··· π4/4A	3.940(6)/3.963(8)	3905/3.904	112.6(3)/110.9(3)

	C_{11}-Cl_4··· $\pi_5/_{5A}$	3.637(6)/3.496(8)	3.606/3.438	111.6(3)/112.9(3)
		H···A (Å)	D···A (Å)	D-H···A (°)
	C_{16}-H···S_{1A}(intra)	2.77	3.163(9)	107
	C_{18}-H···S_1(intra)	2.70	3.086(6)	106
	$C_{23/26A}$-H···Cl_3	2.77/2.77	3.48(1)/3.67(2)	134/162
	C_{27}-H···Cl_6	2.75	3.46(3)	134
	C_{24A}-H···Cl_6	2.74	3.62(3)	158
	C_{18}-H···Cl_4	2.88	3.735(6)	154
TTM-DBT		H···Cg (Å)	D_{pln} (Å)	C-H···Cg (°)
	C_3-Cl_2··· π6	3.411(4)	3.294	162.7(3)
	C_{11}-Cl_4··· π2	3.953(4)	3.450	109.6(4)
		Cl···Cl/S (Å)	C-Cl···Cl/S (°)	Cl/S···C-Cl (°)
	Cl_3···Cl_4	3.366(3)	171.5(2)	106.61
	Cl_7···Cl_4	3.412(3)	133.4(3)	92.1(3)
	Cl_3···Cl_5	3.434(3)	109.3(2)	161.4(3)
	Cl_8···S_1	3.422(2)	158.9(3)	113.3(2)
		H···A (Å)	D···A (Å)	D-H···A (°)
	C_{21}-H···Cl_6	2.967	3.617(6)	128.3
	C_{22}-H···Cl_6	3.007	3.622(7)	125.1
	C_{31}-H···Cl_6	3.020	3.698(7)	131.0

5. Optical spectroscopy

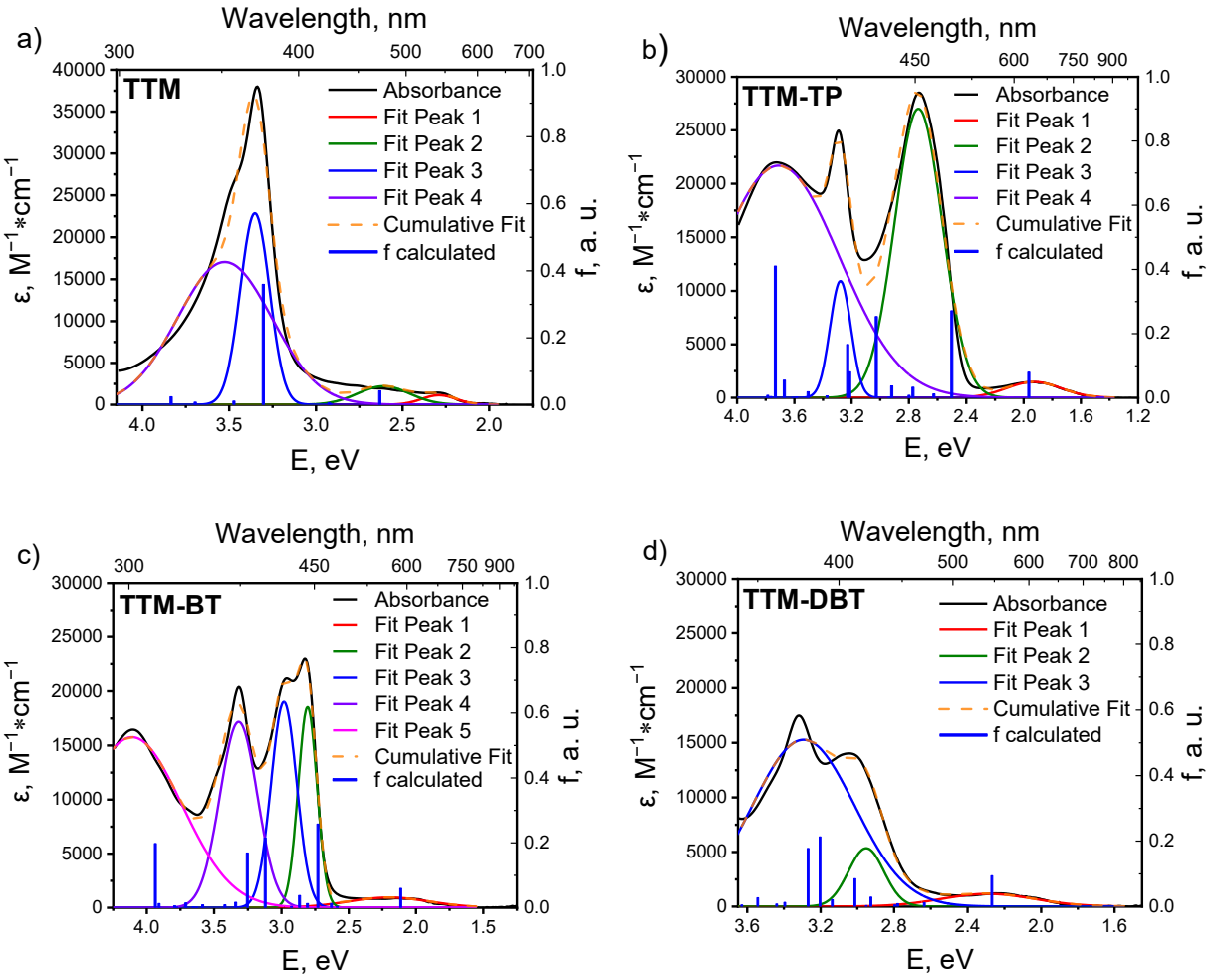

Figure S40. Photophysical data: Absorption spectra of radicals in acetonitrile solution (black), deconvolution of the main absorption bands and corresponding experimental (for D_0-D_1 transition) and theoretical oscillator strengths for a) **TTM**, b) **TTM-TP**, c) **TTM-BT**, d) **TTM-DBT**.

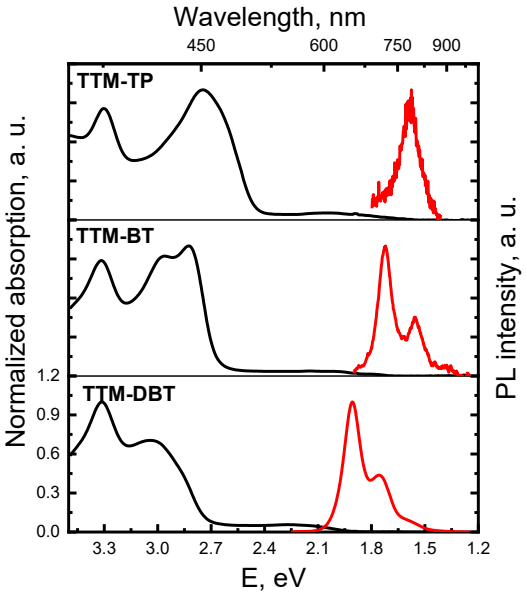

Figure S41. Absorption spectra (black) and PL spectra (red) for the radicals in cyclohexane solution.

Table S8. Optical properties of the radicals in cyclohexane solution.

	Solvent		Cyclohexane	Acetonitrile
TTM-TP	Absorption maxima, nm		328, 375, 452, 610	333, 377, 455, 644
	PL	λ_{max}, nm (eV)	785 (1.58)	805 (1.54)
		PL QY, %	<0.01	<0.01
		FWHM, eV	0.11	0.12
		Stokes shift, eV	0.46	0.39
		τ_{PL}, ns	0.36	0.36
		k_r, ($x10^6$ s^{-1})	<0.28	<0.28
		k_{nr}, ($x10^8$ s^{-1})	27.8	27.8
TTM-BT	Absorption maxima, nm		301, 374, 419, 439, 615	304, 375, 422, 441, 630
	PL	λ_{max}, nm (eV)	719 (1.73), 800 (1.55)	745 (1.66)
		PL QY, %	0.03	0.1
		FWHM, eV	0.08	0.17
		Stokes shift, eV	0.30	0.30
		τ_{PL}, ns	0.60	0.62
		k_r, ($x10^6$ s^{-1})	1.69	1.61
		k_{nr}, ($x10^8$ s^{-1})	16.9	16.1
TTM-DBT	Absorption maxima, nm		375, 408, 544	373, 407, 555
	PL	λ_{max}, nm (eV)	650 (1.90)	680 (1.82)
		PL QY, %	3	4
		FWHM, eV	0.12	0.29
		Stokes shift, eV	0.36	0.41
		τ_{PL}, ns	7.14	9.83
		k_r, ($x10^6$ s^{-1})	5.60	4.04
		k_{nr}, ($x10^8$ s^{-1})	1.34	0.97

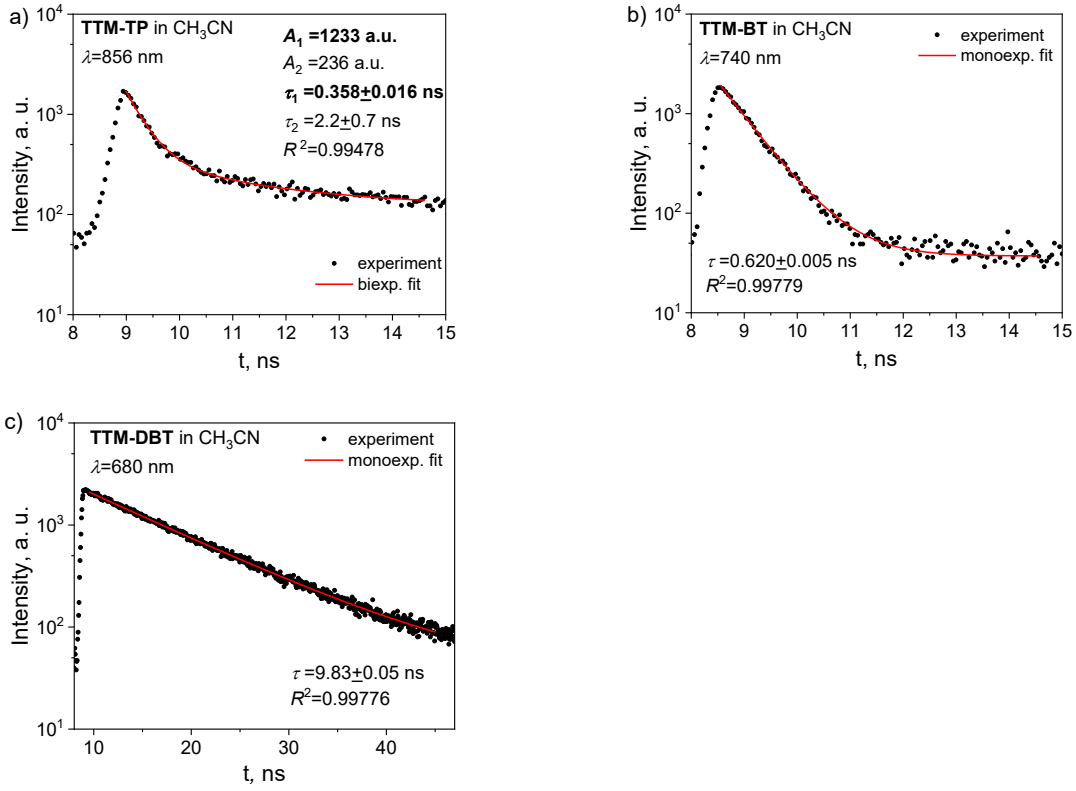

Figure S42. PL kinetics of the radicals in acetonitrile solutions fitted by mono- or biexponential functions at the wavelengths indicated in the plots.

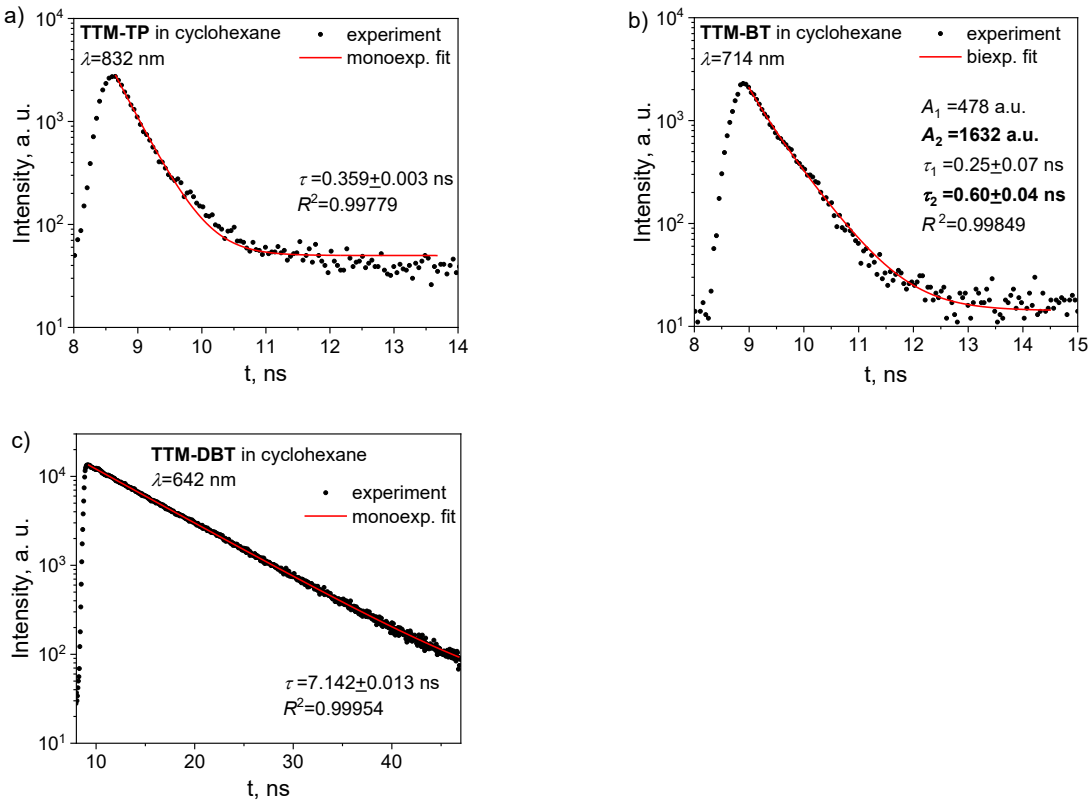

Figure S43. Kinetics of PL of the radicals in cyclohexane solutions fitted by mono- or biexponential functions at the wavelengths indicated in the plots.

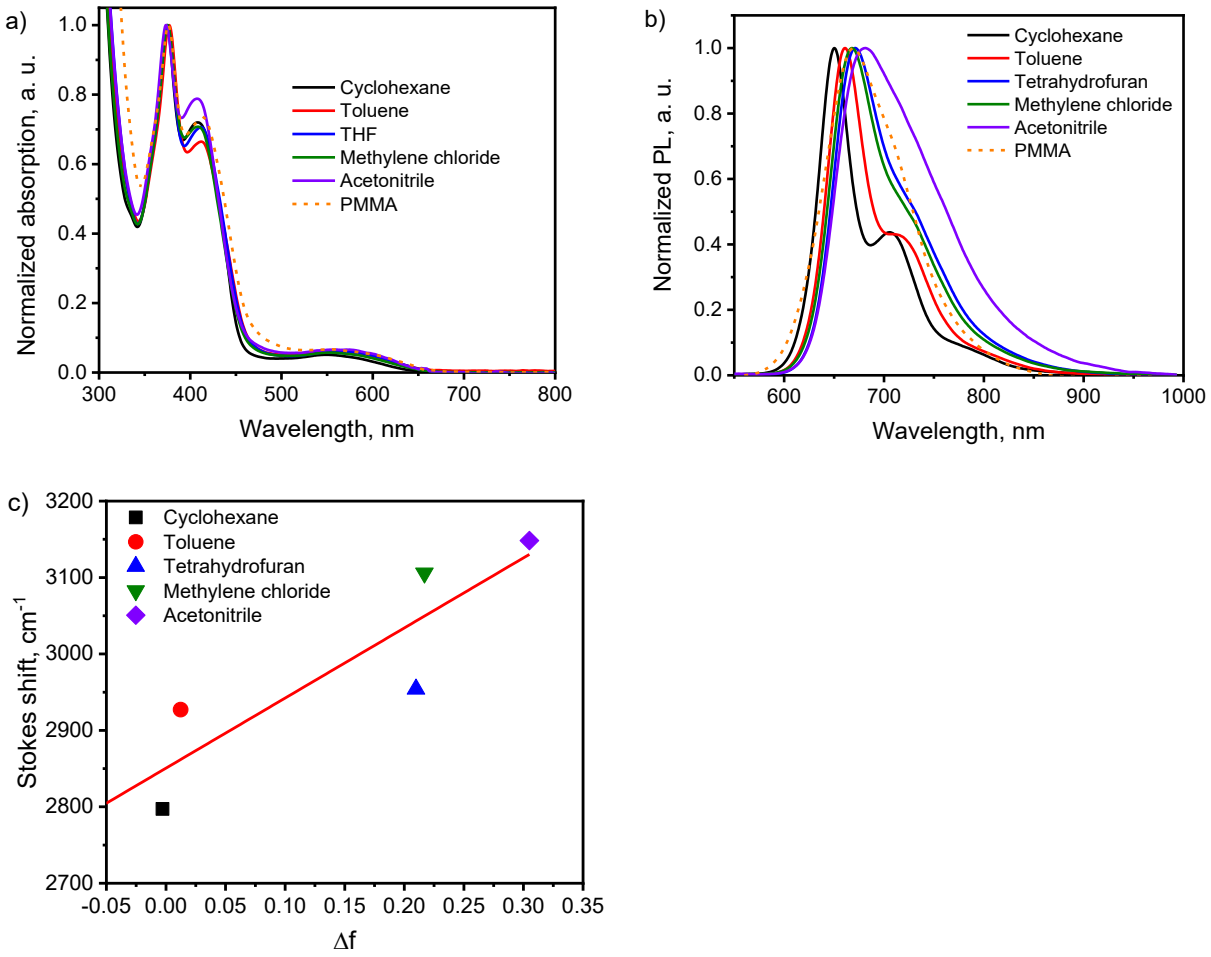

Figure S44. Absorption (a) and PL (b) spectra of **TTM-DBT** in cyclohexane (black), toluene (red), tetrahydrofuran (blue), methylene chloride (green) and acetonitrile (violet) solutions, in PMMA film with 0.7% concentration by weight (orange dash). Plot of the Stokes shifts versus the solvent polarity factor Δf=(ε–1)/(2ε+1)–(n^2–1)/(2n^2+1), where ε is the solvent dielectric permittivity, and n is the solvent refraction index.

6. OLED Data

Experimental details

The OLED device structure was as follows (Fig. S45): glass (1 mm)/ITO (300 nm)/PEDOT:PSS (50 nm)/BT-TBA (15 nm)/light-emitting layer (20 nm)/BCP (8 nm)/Bepq2 (15 nm)/Ca (3 nm)/Al (100 nm).

Substrate cleaning

First, 23x23x1.1 mm glass substrates coated with a patterned ITO layer (transparent anode) were cleaned manually with sodium bicarbonate under water and then in an ultrasonic bath in a surfactant solution at 70°C (30 min). After each of these two stages, the substrates were rinsed with distilled water and dried in nitrogen flow. Further the substrates were treated with radiation from UV lamp Photo Surface Processor PL16-110 (Sen Lights Corporation, 15 mW/cm^2, 254 nm) for 15 minutes.

Layer deposition

PEDOT:PSS was used as the first hole-transport layer, and it was deposited from water suspension by spin coating at 3000 rpm for 120 sec using a Spincoat G3-8 (SCS). The remaining organic layers, namely the second hole-transport layer, light-emitting layer and electron-transport layer, as well as Ca (5 nm)/Al (100 nm) metal cathode, were deposited by vacuum thermal evaporation using a Univex 300 (Leybold) built in a glove box with an inert (N_2) atmosphere (H_2O < 0.1 ppm, O_2 < 5 ppm). The light-emitting layer was deposited by simultaneous coevaporation of the mCP (host) and **TTM-DBT** (dopant) from closely spaced low-temperature evaporators. Temperature of **TTM-DBT** evaporation was 110ºC. The thicknesses of evaporated layers and host-dopant ratio were controlled by thickness monitor TM-400 (Maxtek).

The deposition of organic layers and metal electrodes was carried out at a residual pressure of less than $5 \cdot 10^{-6}$ mbar. For organic layers deposition, samples were placed in a holder located at a height of about 10 cm above the material evaporators. Organic materials were evaporated from a special temperature-controlled evaporator LT Furnace (Luxel) from a quartz crucible. The evaporators for metals were made of tungsten wire. The rate of material deposition on the samples and the thickness of the layers were monitored by a quartz thickness sensor.

To achieve the required 5% doping level in the light-emissive layer, evaporation rate of the host exceeded that of the dopant by a factor of ~20. For this purpose, first the crucible with dopant material was heated and its evaporation rate was stabilized at the level of 0.3-0.4 Å/s, then the crucible with host material was heated to such a temperature that it was evaporated 20 times faster than dopant. The sum of these velocities was monitored by a thickness sensor. Once the co-deposition rate was stabilized, the sample barrier was opened, and the host and dopant materials were deposited on the samples in a predetermined proportion.

During metal cathode evaporation with specific shadow masks, eight round-shaped OLEDs with diameter of 2.2 mm as well as contact pads were formed per one substrate.

OLED characterization

The J-V curves and other characteristics of the OLEDs were measured in a glove box with an inert atmosphere using SourceMeter 2400 (Keithley) controlled by a computer. The EL spectra of the OLED samples were measured using a fiber-input spectrometer with a high-sensitivity CCD array (TRIUS PRO-694 CCD Camera, Strarlight Xpress). For this purpose, the OLED sample was placed under a 10x objective (transparent substrate on top). The OLED emission power was measured using a power meter PM100 with a sensor S120UV (Thorlabs); the light was gathered only from the front face of the device, which was placed as close as possible to a sensor. We estimated the portion of the optical power which hits the sensor as 0.47±0.01, the details are given below.

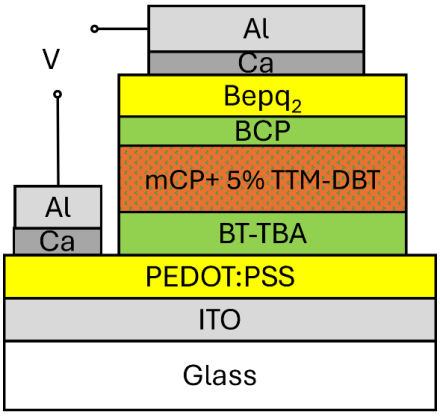

Figure S45. OLED structure.

Estimation of the full OLED EL optical power emitted into the hemisphere

To measure the optical power of OLED EL, the OLED sample was placed as close as possible to the photodetector sensor. However, in such a configuration, not all the light, emitted from the OLED front face into the hemisphere, reaches the photodetector active area. Moreover, a significant portion of light does not fall normally (i.e., at the right angle) to the surface of the photodetector active area. Since the photodetector used was designed and calibrated to measure optical power at normal incidence, the power values measured in our configuration are lower than the full optical power of the light emitted by OLED sample from its front face into the hemisphere. To estimate the ratio between the measured and full optical power, we measured the OLED optical power, placing the sensor far enough from the sample so that the EL hits the sensor surface almost at the normal incidence. Then, we calculated the full optical power from the measured value in assumption of a Lambertian radiation pattern. Finaly, the full EL power emitted into the hemisphere was calculated taking into account the ratio between the measured optical power values in the cases when the OLED was placed close to the sensor and far from it.

Supplementary Note S3. OLED characterization results

Figure S46 shows current-voltage characteristics for the OLED based on **TTM-DBT** and the corresponding voltage dependence of EL EQE. The current-voltage characteristic had a typical diode I-V curve with opening voltage of about 5 V, and the maximum EL EQE value was 0.043% and reached at ~ 6 V. The main characteristics of the OLEDs fabricated are summarized in Table S9. The EL spectrum was attributed to emission from the **TTM-DBT** since the maxima of the EL and PL spectra are close (Fig. 4d). However, the EL spectrum has a small contribution from emission of the host and transport layers (see below Fig. S47a). If emission from the host and transport materials would be avoided in a more optimized OLED structure, the **TTM-DBT** OLEDs can potentially show reasonably pure deep-red emission as follows from Fig. 4f; the CIE coordinates are also listed in Table S9.

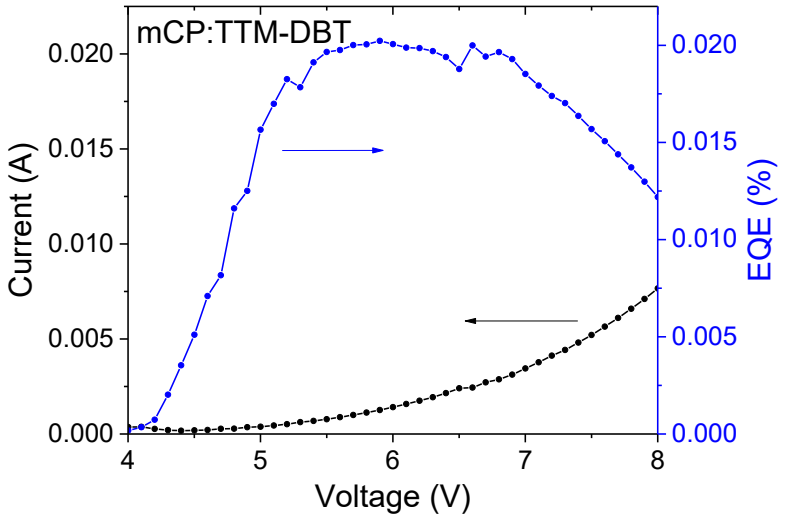

Figure S46. Current-voltage characteristics and EQE voltage dependences for the mCP:**TTM-DBT** OLED.

OLEDs without dopant (reference sample)

As reference samples, the devices based on the pristine host material, mCP, prepared and characterized in the same conditions as the doped ones, the structure of devices without dopant was as follows: ITO/PEDOT:PSS/BT-TBA/mCP/BCP/Bepq2/Ca/Al. Its EL spectra had two peaks at 512 nm and 405 nm. The maximal EL EQE is reached at voltages slightly higher than 8 V and equal to 0.043%. The typical brightness values for these devices were about 96 cd/m^2 at current density values of about 200 mA/cm^2.

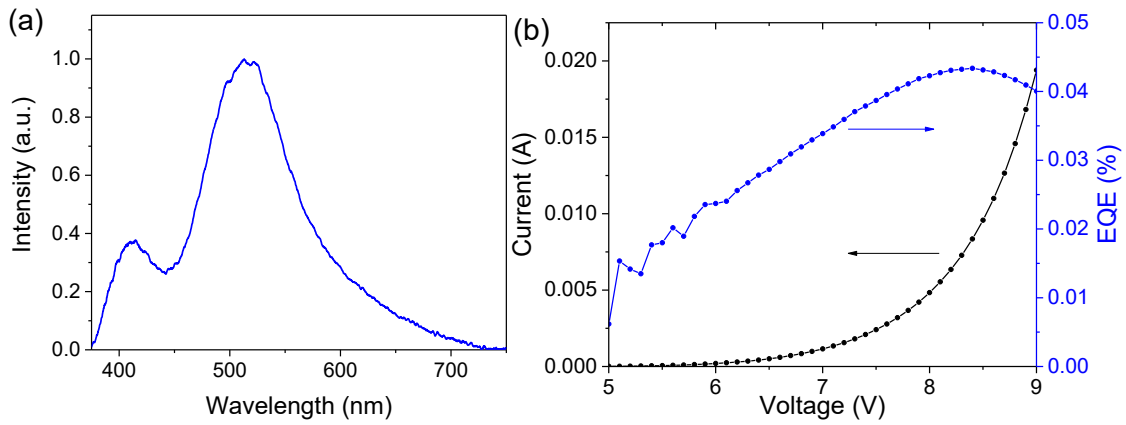

Figure S47. OLED based on the pristine host material, mCP (i.e., without dopant): EL spectrum (a), typical current-voltage characteristics and EQE voltage dependence (b).

Table S9. Data for the OLEDs fabricated.

Emission layer	λ_{max}, nm	FWHM, nm	CIE x	CIE y	EQE, %	PCE, %	L, cd/m^2	Curr.Eff., cd/A	Ener.Eff., lm/W
mCP:**TTM-DBT**	674	84	0.59	0.35	0.043	0.015	2.3	0.009	0.009
mCP	512	97	0.26	0.43	0.043	0.013	96	0.043	0.038

7. Photostability

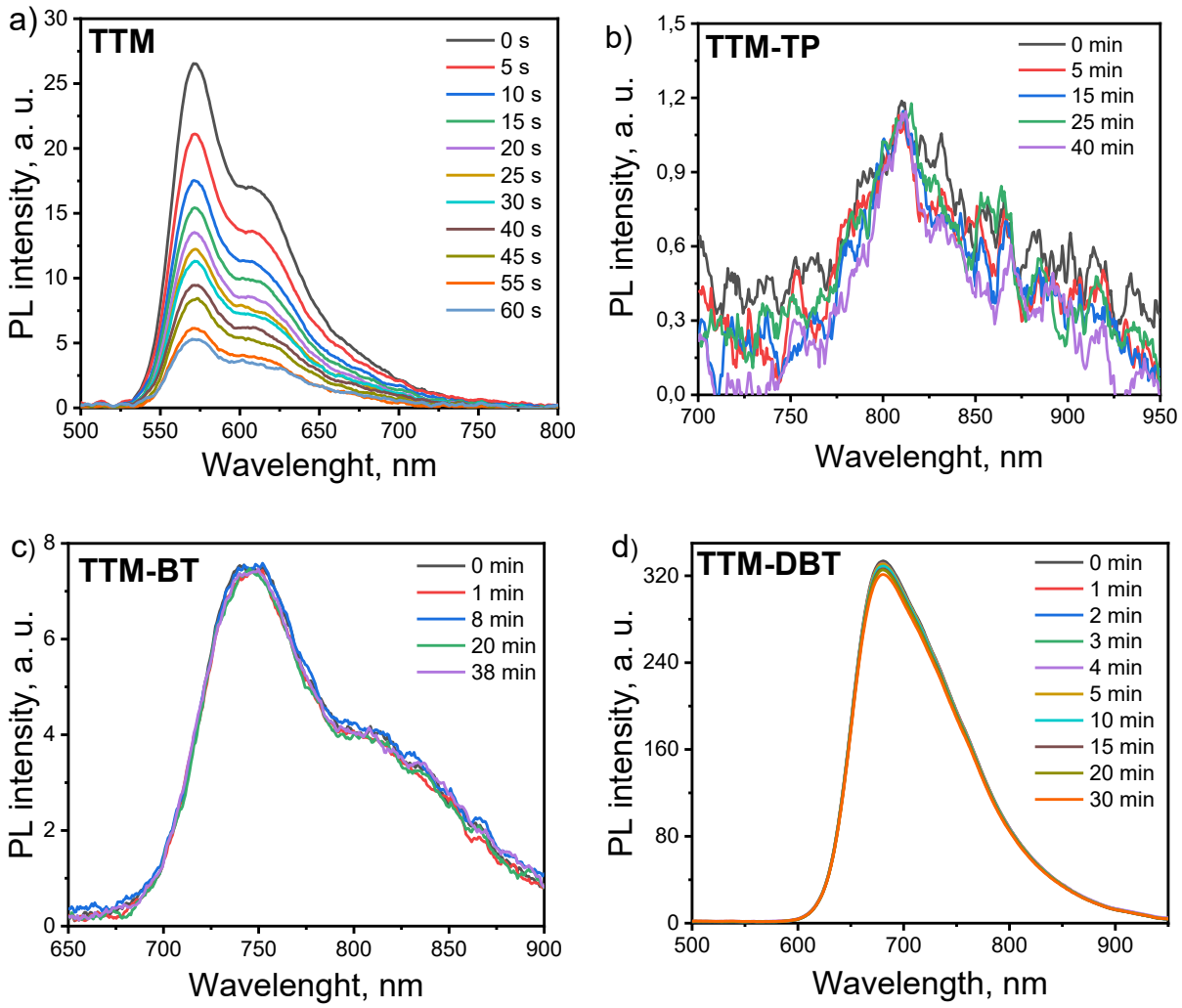

Figure S48. Time-dependent PL spectra of radicals in deaerated acetonitrile solution (C=10^{-6} M).

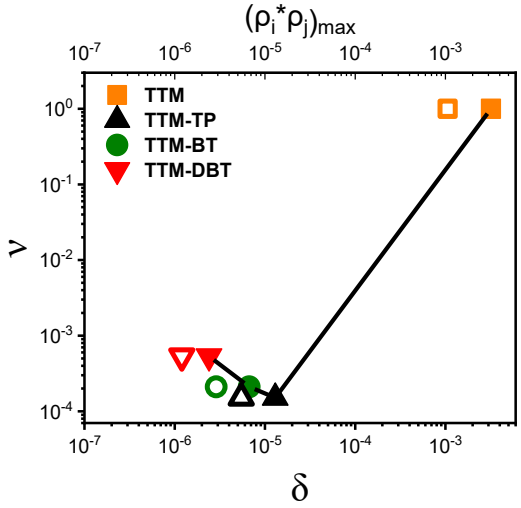

Figure S49. The dependence of photodegradation rate ν on the δ (filled symbols) and the maximal value ($\rho_i \cdot \rho_j$) (open symbols).

References

1. C. Lee, W. Yang and R. G. Parr, *Phys. Rev. B. Condens. Matter.*, 1988, **37**, 785-789.
2. P. C. Hariharan and J. A. Pople, *Theor. Chem. Acc.*, 1973, **28**, 213-222.
3. T. Clark, J. Chandrasekhar, G. W. Spitznagel and P. V. R. Schleyer, *J. Comput. Chem.*, 1983, **4**, 294-301.
4. F. M. Bickelhaupt and E. J. Baerends, *Rev. Comput. Chem.*, 2000, **15**, 1-86.
5. R. Krishnan, J. S. Binkley, R. Seeger and J. A. Pople, *J. Chem. Phys.*, 1980, **72**, 650-654.
6. M. J. Frisch, J. A. Pople and J. S. Binkley, *J. Chem. Phys.*, 1984, **80**, 3265-3269.
7. C. Adamo and V. Barone, *J. Chem. Phys.*, 1999, **110**, 6158-6170.
8. A. D. Becke, *J. Chem. Phys.*, 1993, **98**, 1372-1377.
9. T. Yanai, D. P. Tew and N. C. Handy, *Chem. Phys. Lett.*, 2004, **393**, 51–57.
10. Y. Zhao and D. G. Truhlar, *Theor. Chem. Acc.*, 2008, **120**, 215-241.
11. G. M. J. Barca, C. Bertoni, L. Carrington, D. Datta, N. De Silva, J. E. Deustua, D. G. Fedorov, J. R. Gour, A. O. Gunina, E. Guidez, T. Harville, S. Irle, J. Ivanic, K. Kowalski, S. S. Leang, H. Li, W. Li, J. J. Lutz, I. Magoulas, J. Mato, V. Mironov, H. Nakata, B. Q. Pham, P. Piecuch, D. Poole, S. R. Pruitt, A. P. Rendell, L. B. Roskop, K. Ruedenberg, T. Sattasathuchana, M. W. Schmidt, J. Shen, L. Slipchenko, M. Sosonkina, V. Sundriyal, A. Tiwari, J. L. Galvez Vallejo, B. Westheimer, M. Wloch, P. Xu, F. Zahariev and M. S. Gordon, *J. Chem. Phys.*, 2020, **152**, 154102.
12. M. G. Voronkov and F. D. Faitel'son, *Chem. Heterocycl. Compd.*, 1967, **3**, 182–185.
13. D. Liu, H. Ren, L. Deng and T. Zhang, *ACS Appl. Mater. Interf.*, 2013, **5**, 4937-4944.
14. V. Gamero, D. Velasco, S. Latorre, F. López-Calahorra, E. Brillas and L. Juliá, *Tetrahedron Lett.*, 2006, **47**, 2305-2309.
15. A. M. Brouwer, *Pure Appl. Chem.*, 2011, **83**, 2213-2228.
16. M. S. Kazantsev, E. S. Frantseva, L. G. Kudriashova, V. G. Konstantinov, A. A. Mannanov, T. V. Rybalova, E. V. Karpova, I. K. Shundrina, G. N. Kamaev, M. S. Pshenichnikov, E. A. Mostovich and D. Y. Paraschuk, *RSC Adv.*, 2016, **6**, 92325-92329.
17. SAINT, Data Reduction and Frame Integration Program for the CCD Area-Detector System, Bruker Analytical X-ray Systems: Madison, Wisconsin, USA, 1997–2006.
18. G. M. Sheldrick, SADABS, Program for area detector adsorption correction, Institute for Inorganic Chemistry, University of Goettingen: Goettingen, Germany, 1996.
19. G. M. Sheldrick, *Acta Crystallogr. A*, 2008, **64**, 112-122.
20. G. M. Sheldrick, *Acta Crystallogr. C*, 2015, **71**, 3-8.
21. O. V. Dolomanov, L. J. Bourhis, R. J. Gildea, J. A. K. Howard and H. Puschmann, *J. Appl. Crystallogr.*, 2009, **42**, 339-341.
22. A. L. Spek, *Acta Crystallogr. D*, 2009, **65**, 148-155.
23. C. F. Macrae, P. R. Edgington, P. McCabe, E. Pidcock, G. P. Shields, R. Taylor, M. Towler and J. van de Streek, *Appl. Crystallogr.*, 2006, **39**, 453-457.